Chapter 5

8–13 μm spectroscopy of YSOs: Evolution of the silicate emission feature

Abstract

In this study, 8–13 μm spectra of $\sim$ 20 stars ranging from YSOs to debris disks and spectral types from A to M were obtained using the Long Wavelength Spectrometer at the W. M. Keck Observatory. The evolution of the silicate feature from absorption in young, embedded sources, to emission in isolated stars and complete absence in older "debris" disks seen in ISO observations of high/intermediate-mass YSOs (Meeus & Waelkens, 1999) is extended here to $\sim$ solar mass stars. In a few objects, the silicate feature is more complex, with absorption near 9.5 μm and emission peaking around 10.3 μm. These sources appear to be at a transitional stage where the star is just becoming visible in the optical. In addition, there appears to be a marked difference between intermediate mass Herbig Ae stars and solar mass T Tauri stars of the same age. For some, but not all, of the Herbig Ae stars in the sample, the emission feature has a bump at $\sim$11 μm, similar to the emission from crystalline silicates seen in comets and the debris disk β Pictoris. All of the T Tauri stars, however, show the classical emission/absorption features which have been attributed to amorphous silicates, although some T Tauri stars show a silicate feature which is much broader than that from the diffuse ISM. It is unclear whether crystalline silicates are truly absent in T Tauri stars, for colder or larger crystalline silicate grains would not emit strongly in the 8–13 μm region, but may be visible through far-infrared lattice modes accessible from space born observations.

5.1 Introduction: Silicates and star formation

Models of dust condensation processes from an initially hot gas (Grossman, 1972, Gail, 1998; Finocchi et al., 1997; Finocchi & Gail, 1997) suggest that grains in the interstellar medium, and thus in the early stages of star formation, are primarily composed of amorphous silicates, particularly olivines ($Mg_{2x}Fe_{(1-x)}SiO_4$, or ortho-silicates), ranging from fayalite ($x = 0$) to forsterite ($x = 1$), and orthopyroxenes ($Mg_xFe_{(1-x)}SiO_3$, or meta-silicates), ranging from ferrosillite ($x = 0$) to enstatite ($x = 1$). Conversions between Fe and Mg dominated silicates are controlled by the reactions,

$$MgSiO_3(s) + (1-x)Fe \leftrightarrow Mg_xFe_{(1-x)}SiO_3(s) + (1-x)Mg \tag{5.1}$$

$$Mg_2SiO_4(s) + 2(1-x)Fe \leftrightarrow Mg_{2x}Fe_{2(1-x)}SiO_4(s) + 2(1-x)Mg, \tag{5.2}$$

such that at high temperatures, the iron component is essentially distilled off from the solution, leaving olivines that are nearly pure forsterite and orthopyroxenes that are nearly pure enstatite– substantial amounts of ($Fe_{1-x}SiO_{3,4}$) remain only at T < 200 K. In a gas of solar composition, transitions between the ortho- and meta-silicates occur via the reaction,

$$Mg_2SiO_4(s) + H_2(g) \leftrightarrow MgSiO_3(s) + Mg + H_2O, \tag{5.3}$$

such that the conversion is controlled by

$$f_o = \frac{\epsilon_{Mg} - \epsilon_{Si} K_c^3 K_p}{(2 + z - (1+z)K_c^3 K_p)\epsilon_{Si}}, \tag{5.4}$$

where f_o is the fraction of ortho-silicates, z is the ratio of meta- to ortho-silicates, ϵ_{Mg} and ϵ_{Si} are the abundances of Mg and Si (relative to H), and K_c and K_p are equilibrium constants for reaction 5.3 at standard concentration and constant pressure. Thus, the fraction of meta- versus ortho-silicates depends on both the temperature and pressure and only for a very narrow region in P-T space does the ortho-silicate (i.e., forsterite) form a significant fraction of the mixture. For a given pressure, the meta-silicate (i.e., enstatite) dominates at low temperatures and decreases with increasing temperature if equilibrium prevails.

Interstellar dust consists of particles from wide range of sources (stellar atmospheres, novae, supernovae). Olivine dominates over orthopyroxene, observationally, and high-energy rays and low temperatures are expected to result in amorphous mixtures of the two. Indeed, strong, smooth features at 9.7 and 18.5 μm, corresponding to the Si-O stretching and bending modes, respectively, are observed to arise from absorption of background light by dust in the diffuse interstellar medium (Bouwman et al., 2001). Molecular clouds also possess a mixture of amorphous olivine and pyroxene, which may be covered with carbonaceous or organic material and ice at sufficiently high extinctions (i.e., densities; Gibb et al., 2000). Silicates are expected to be amorphous in molecular clouds as well, due to cosmic ray impacts, and a broad structureless band centered at 10 μm is observed toward several objects. In contrast, solar system dust (cometary grains, IDPs, CAIs) and dust surrounding main sequence stars contain crystalline silicates, with olivine and enstatite as the dominant components, similar in composition (but not structure) to star-forming regions. The crystallization process is believed to be predominantly thermally controlled. At high temperatures (T$\sim$1200 K), annealing of anhydrous silicates begins with thermal diffusion of impurities, with mobilities dependent on atomic size. The impurities assemble, leaving local order and microcrystalline lattice structures within the silicates. If the annealing lasts a suffuciently long time, or if the temperatures are hot enough, crystallization begins at critical nuclei. In laboratory experiments, silicate smokes annealed at T = 1200 K develop local order in domains of 1 nm within 1 day (Nuth & Donn, 1982). The evolution of a silicate grain with increasing temperature is expected to proceed as follows (Gail, 1998),

$$amorphous \rightarrow polycrystalline \rightarrow enstatite \rightarrow forsterite. \tag{5.5}$$

The presence of crystalline silicates is thus expected in high-temperature condensates in meteorites, such as CAIs. IDPs are produced by impacts, collisions and/or disintegrations of small bodies and the release, by sublimation, of refractory grains frozen in cometary nuclei, so the presence of crystalline silicates can also be easily explained in these particles. Short- and long-period comet spectra show emission from both crystalline and amorphous silicates, though the crystalline fraction can vary significantly (Hanner et al., 1994; Knacke et al., 1993; Skinner et al., 1992; Fajardo-Acosta et al., 1993; Knacke et al., 1993; review by Wooden, 2002). These results are particularly interesting as they indicate that although some crystalline material may be made when comets pass close to the sun, a substantial fraction must have been crystallized before comets were formed. The abundances of crystalline silicates found in some comets are too high (up to 30%), however, to be accounted for by crystalline silicates in the ISM (<5%), indicating that they were formed around protostars, most likely in circumstellar disks. The presence of crystalline silicates in *both* short- and long-period comets further suggests the presence of long range mixing processes required to bring crystalline grains (annealed at >1000 K) into the colder parts of the disk in which comets form.

Clearly, planet-forming disks are the place to look for the *in situ* crystallization of silicates. In the simplest scenario, amorphous silicates from the interstellar medium enter the accretion disk and are modified depending on their distance from the star, with crystallization of the dust dependent on the exposure to stellar radiation or the age of the disk. The silicates in the outer disk are expected to accrete icy mantles and retain cores that are similar to ISM dust, composed primarily of amorphous olivine and pyroxene. In warmer regions ($T > 1000$ K), annealing leads to crystallization. The diffusion processes start in regions relatively close to the star (the exact distance depends on the stellar luminosity), and result in the conversion of the amorphous lattice structure. At radii corresponding to temperatures above 1000 K, the dust grains should possess regions of localized crystallization that are detectable in the IR; at radii corresponding to $T > 1500$ K, 0.1–1 μm grains should be completely crystallized.

The properties of dust grains in accretion disks therefore must be significantly modified with respect to those of the ISM in order to reproduce silicate observations (D'Alessio et al., 2001). The observed differences in the silicate spectra of interstellar versus solar system dust appears to be an evolutionary sequence, in which the composition of the grains gradually changes from amorphous olivine to crystalline forsterite (as noted above) during the star formation process. Data returned from the Infrared Space Observatory (ISO) enabled the detection of spectra from several intermediate mass (>1 $M_\odot$), Herbig Ae/Be protostars (hereafter referred to as HAEBE) at a range of ages and stellar evolutionary stages, and an evolutionary sequence based on the 2 to 45 μm spectrum has been suggested (Meeus & Waelkens, 1999). The sequence begins with rising featureless spectra indicative of dense cloud cores (i.e., Cep A IRS6); spectra in the second category possess strong absorption by amorphous silicates near 10 μm and are attributed to embedded protostars (Z CMa). Emission from warm silicates near 10 μm and prominent cold dust emission longward of 15 μm (HD 100546) defines the third category, which is likely composed of objects with optically thick protoplanetary disks (known as Class II objects). For several sources (i.e., HD 104237; category 4), warm silicate emission is seen without the cold component and is interpreted as arising from disks undergoing planet formation. Finally in the oldest sources, the spectrum is close to photospheric (i.e., HD 139614) indicating dispersal of most of the circumstellar dust.

ISO and ground based observations have detected crystalline silicate emission bands (11.3, 27.5, 33.5, 35.8 and 70 μm) toward a large sample of class II HAEBE stars (Molster et al., 1999; Meeus et al., 2001) and toward the "debris" disk β Pictoris (Knacke et al., 1993). The emission bands at 27.5, 33.5, 35.8 and 70 μm are highly dependent on the structure of the dust and these studies show large variations in dust crystallinity and composition among YSOs of similar age and stellar properties (Meeus et al., 2001; van den Ancker et al., 2000), indicating the necessity for large samples for the determination of a general theory of disk evolution. However, the differences between the silicate emission features in HAEBE are complex functions of the grain size and composition as well as the disk morphology and optical depth (Meeus et al., 2001; Bouwman et al., 2003; van Boekel et al., 2003). The emission features arising from the dust in HAEBE star disks can be reproduced by models with varying amounts of olivine, forsterite, enstatite and silica and with mixtures of 0.1–2 μm sized grains. Additionally, it was found that grain shape plays a large role in the interpretation of silicate spectra, particularly for strong crystalline bands (Fabian et al., 2001). A combination of spherical and ellipsoidal grains are required to reproduce observed spectra.

Observations from the ISO satellite also indicate the presence of two distinct end member dust populations in the young star HD 142527 (Malfait et al., 1999), including warm (500–1500 K), crystalline silicates with narrow features at 11.3 μm and cold (30–60 K), hydrous semi-crystalline silicates (silicate layers separated by layers of cations and interstitial water), with strong, broad emission that contributes to the far-IR continuum longward of 50 μm. Additionally, large amounts of crystalline water ice are indicated from strong emission features around 44 and 55 μm. Although the amorphous-to-crystalline transition requires high temperatures (T$\sim$1500 K), several other young stars also have been shown to possess cold crystalline silicates (i.e., HD 100546; Bouwman et al., 2003). These observations and those of crystalline silicates in comets indicate that radial mixing may be important as a method of transfer material outward from the warm, inner regions of the disk. Mechanisms for cold crystallization processes have also been suggested. For example, observations indicating copious amounts of water ice and hydrous silicates have been used to suggest aqueous alteration of grains as a crystallization mechanism in circumstellar disks. Collisions might also transiently generate high densities and/or temperatures in the outer disk, which could lead to crystallization in the Class II/III phase.

Observations of silicate emission from older stars have been particularly revealing. As small dust is expected to be cleared from T Tauri and Herbig Ae disks on timescales less than 10^7 years, the material in disks older than 10^7 yr is expected to be "second generation" debris from the collision of planetesimals. β Pictoris is a late type (12^{+8}_{-4} Myr; Zuckerman et al., 2001) A star, whose IR and optical (HST) images have been fit with the model of a warped disk, thought to be indicative of planet formation (Mouillet et al., 1997; Weinberger et al., 2003). The IR spectrum observed (Knacke et al., 1993) exhibits a remarkable resemblance to that of solar system grains and comets, suggesting the presence of a mixture of crystalline and amorphous material and a possible connection between the crystallization of silicates and the formation of planets. Recently, spatially resolved IR spectroscopy of β Pic (Weinberger et al., 2003) revealed that the silicate emission arises only from dust within $0''.8$ of the star. Furthermore, the dust composition (a mixture of amorphous and crystalline dust) appears to remain constant throughout this region. Models of the dust in the disk surrounding the HAE star HD 100546 have been used to demonstrate that collisional destruction of differentiated objects is a possible production mechanism for small crystalline grains. This hypothesis is supported by an absence of thermal contact between the chemical constituents of the dust and an increase in the fraction of crystalline silicates with *increasing* distance from the star. The presence of substantial emission from a small grains ($<$10 μm) with temperatures of $\sim$200 K suggest a puffed up disk at 10 AU from the star, supporting the idea that the disk has been cleared by planet formation processes.

Although ISO observations have significantly improved our understanding of the composition of circumstellar dust, there are still many questions to be answered. For the most part, due to lack of sensitivity, the ISO observations probed only disks around relatively high-mass, luminous stars. It is unclear whether the dust compositions or disk morphologies will be similar for $\leq$solar mass stars. The large collecting area and therefore increased point source sensitivity of ground based telescopes make them especially valuable tools in the detection of silicate emission from low-mass young stellar objects, which were virtually unprobed by ISO. Additionally, high spectral resolution studies of the warm dust emission (near 10 μm) are vital in understanding the processing of dust necessary to produce the two populations discussed above and observations of mid-infrared dust emission are a useful means of investigating the dust composition in the pivotal planet-forming region (1–10 AU) of circumstellar disks around young stars. Ground based observations are limited to $\lambda \leq 20$ μm, and so such studies also serve a pathfinder role for subsequent space borne observations with the next generation of cooled observatories (i.e., SIRTF and ASTRO-F).

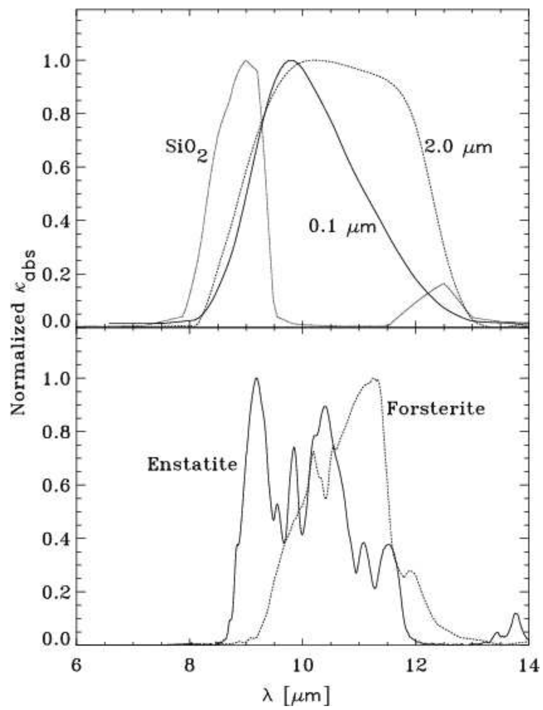

Figure 5.1 The emission properties of silicate dust grains (from Bouwman et al., 2001). Absorption coefficients are normalized and plotted vs. wavelength. The top panel shows emission from quartz and from amorphous olivine grains of two different sizes. The bottom panel shows emission from enstatite and forsterite crystals.

The dominant feature in the 8–13 μm spectrum is emission from amorphous olivine (peaking at 9.5 μm), with smaller emission features arising from silica (SiO_2; 8.6 μm) and crystalline enstatite ($MgSiO_3$; 9.2, 10.4 μm) and forsterite (Mg_2SiO_4; 10.2, 11.3 μm).[1] Thus, the trend from amorphous olivine to crystalline forsterite results in a shift of the 10 μm silicate emission feature from 9.7 to 11.3 μm (see Figure 5.1). Usually, the shift between the emission features of amorphous olivine and the 11.3 μm emission from crystalline forsterite is referred to as the amorphous-to-crystalline transition and used to classify the amount of amorphous-to-crystalline material in the disk. This sort of analysis is complicated by the fact that the strength of the silicate emission features cannot be uniquely correlated with the abundance of silicates in the disk. The presence of organics can increase the opacity at $\lambda < 6$ μm and decrease the contrast between the silicate band at 10 μm and the adjacent continuum (D'Alessio et al., 2001). Also, the width of the amorphous olivine emission feature increases substantially with grain size, with peaks decreasing in strength and spreading from 9.7 to 12 μm for grain sizes of 2 μm (van Boekel et al., 2003). For large grains ($a_{max} > 1$ mm), the

[1] The peak positions described above are for 0.1 μm grains (Meeus et al., 2001).

silicate bands at 10 and 20 μm almost disappear entirely (Fabian et al., 2001). Additionally, the interpretation of emission in the 10 μm atmospheric window is complicated by the fact that ground based observations do not have enough spectral coverage to establish a reasonable continuum. The IR flux from the disk varies greatly from source to source, is often not constant across this window, and can have a large effect on the shape of the observed spectrum. There are therefore many methods which have been implemented to calculate and subtract the continuum, but a standard method has not been established.

There have been a number of surveys of ground based 8–13 μm emission from T Tauri star disks. Early surveys of emission from disks around T Tauri stars (Cohen & Witteborn, 1985; Hanner et al., 1998) appeared to indicate that the spectra of young, low-mass stars resembles that of molecular clouds, which show a rather sharp, single peak between 9 and 10 μm, very similar to that seen in the ISM, and may indicate that the dust surrounding these low-mass objects has not undergone significant processing during the collapse of the cloud and evolution of the circumstellar disk. However, 5.9–11.7 μm spectra of 9 low mass sources in Chameleon (Natta et al., 2000) display emission which is significantly broader and stronger than that of the diffuse ISM, especially at the edges of the silicate feature at 8.5 and 11.3 μm, for all stars in the sample. PAHs are not believed to significantly contribute due to the absence of standard PAH emission features at 3.3, 6.2 and 7.6 μm. Approximating the continuum using a powerlaw normalized in the 5.8–8 μm spectral region, Natta et al. (2000) find typical ratios of L_{sil}/L_* of 1–2% (except glass Ia, 10%). They also find that the spectra are consistent in 6 of 9 cases with the luminosities predicted by a simple radiation transfer model of a flared disk in hydrostatic equilibrium similar to that of Chiang & Goldreich (1997). For this model, they adopt the cross section of pyroxene, but the data can also be fit with varying compositions of olivine and pyroxene, for dust sizes of less than 1 μm (or pyroxene alone with larger grains $\sim$1 μm in size).

5.2 Sample selection

In this study, the spectra of the silicate emission feature at 10 μm toward several Herbig Ae and T Tauri objects were acquired at R = 100, using the Long Wavelength Spectrometer at the W. M. Keck observatory. The goal was to use the spectra to characterize the composition of the dust, particularly the dominance of silicates versus PAHs and the degree of crystallinity of the silicate grains present. Objects with varying age and mass were chosen in order to put this information in context with the stellar evolutionary process for both low and high-mass stars. Ten embedded YSOs were observed, including seven low mass stars chosen from Kenyon et al. (1993) and 3 well known high-mass YSOs, the Becklin Neugebauer object (BN), NGC 2024 IRS 2, and MonR2 IRS3 to provide "internal calibrants" for this study. The latter observations should also probe the composition of

Table 5.1. Source parameters for Class II and Class III sources

Source	RA(J2000)	DEC(J2000)	d(pc)	M_* ($M_\odot$)	L_* ($L_\odot$)	T_{eff} (K)	Sp.Type	Age (Myr)	R_* ($R_\odot$)	Ref.
49 Cet	01 34 37.78	-15 40 34.9	61	2.4g	23.44	9333	A1V	7.8	2.30	1
HD 17925	02 52 32.129	-12 46 10.972	10.4	0.8g	-	5000	K1V	80	0.82g	3
HD 22049	03 32 55.844	-09 27 29.744	3.3	0.78g	-	5000	K2V	330	0.8g	3,4
AA Tau	04 34 55.2	+24 28 52	140	-	0.71	3981–4000	K7	2.4	0.7g	5
LkCa 15	04 39 17.8	+22 21 03	140	0.97	0.724	4350–95	K5:V	6.6–11.7	0.72	6,7
GM Aur	04 55 10.2	+30 21 58	140	0.84	0.741	4730	K5V:e	1.8	1.78	6,7,8
MWC 480	04 58 46.27	+29 50 37.0	131	2.3	23.7	8890	A2	4.6	2.1	7,9
HD 233517	08 22 46.71	+53 04 49.2	23–40	-	0.20	4170–4500	K2–K7	-	0.7g	-
Hen 3-600A	11 10 27.9	-37 31 52	50.0	0.25	0.23	3388	M3	1.0	0.45g	10,11,12
HD 102647	11 49 03.578	+14 34 19.417	11.1	2.0g	-	8720	A3V–A8	240	2.01	4
HR 4796A	12 36 01.032	-39 52 10.219	76	2.5	35	10000	A0V	-	2.6g	13
IRAS 14050-4109	14 05 05.7	-41 09 40	-	-	-	4406	K5	-	1.39	-
HD 163296	17 56 21.29	-21 57 21.9	120	2.4	35.2	9475	A1V	5.0	2.2	9
HD 179218	19 11 11.254	+15 47 15.630	240^{+70}_{-40}	4.0	221.9	10220	B9/A0/IV/Ve	0.3	4.7	15,16$^{\infty}$
WW Vul	19 25 58.75	+21 12 31.3	550	2.9	43	8600	A3e/B9V	-	2.4	17
HD 184761	19 34 58.97	+27 13 31.2	65	2.0g	18.3g	7500	A8V	-	1.5g	18
HD 216803	22 56 24.0529	-31 33 56.042	7.70	-	-	4500	K4V	-	-	-

Note. — References: 1-Sylvester et al. (1996), 2-White & Ghez (2001), 3-Habing et al. (2001), 4-Glass (1975), 5-Thi et al. (2001), 6-Qi (2001), 7-Simon et al. (2001), 8-Kenyon & Hartmann (1995), 9-Mannings & Sargent (1997), 10-Geoffray & Monin (2001), 11-Kastner et al. (1997), 12-de La Reza et al. (1989), 13-Jura et al. (1993), 14-Natta et al. (1997), 15-Mannings & Sargent (2000), 16-van den Ancker et al. (1998), 17-Natta et al. (2001), , 18-Miroshnichenko et al. (1999), 19-Friedemann et al. (1995), 20-Hillenbrand et al. (1992).

largely unprocessed grains and absorption from amorphous silicates is expected. There are ten class II T Tauri and Herbig Ae stars in the sample, most of which have been studied extensively at other wavelengths and have very well characterized SEDs. ISO observations indicate that at least two Herbig Ae stars in this sample, HD 163296 and WW Vul, possess detectable amounts of crystalline silicates. As discussed above, silicate crystallization is likely occurring at this intermediate stage of stellar evolution and we would expect the most variation of crystalline silicate content with age or luminosity in this part of the sample. Seven debris (Class III) disks were also included, as classified by their optically thin IR continuum and ages older than 6 Myr and are the most likely candidates for detection of crystalline silicates, provided warm dust is present.

5.3 Photometric and spectroscopic observations

8–13 μm spectra and photometry for several intermediate and low mass stars were obtained using Long Wavelength Spectrometer (LWS) at the W. M. Keck Observatory between August 1999 and June 2000 (Table 5.2). LWS provides diffraction-limited imaging (10$''$ field of view, 0.$''$08/pixel) and spectroscopic (R = 100–1400) capabilities in the 3–25 μm wavelength range. Photometry was obtained with the 10.7 μm filter ($\Delta\lambda$ = 10.0–11.4 μm) during the nights of Feb 20–21 and Dec 9, 2000, for which the seeing was poor and variable: 0.$''$3–0.$''$6 at 10 μm (the diffraction limit is 0.$''$22). For the spectroscopic observations, the *Nwide* filter and low resolution grating (LRES) were used to obtain 8.1–13 μm spectra, with R = 100, at a dispersion of 0.037 μm/pixel. Slit widths of 3 and 6 pixels were used, resulting in 0.$''$24 and 0.$''$48 apertures, respectively. Sources were imaged prior to each spectroscopic observation to ensure optimal placement within the slit. For most spectroscopic observations, additional calibration scans were obtained using the Keck routine *LSEC*, in which the data is chopped between an ambient blackbody source (T≈274 K, the temperature of the telescope) and the sky. After normalization, these data were used as a spectral flat field in order to calibrate out grating abnormalities. Dome flats and darks were taken at the end of each night with exposure times equal to those on source. The raw six-dimensional LWS data, consisting of two nod-chop pairs, were coadded into two-dimensional images (Figure 5.2), using the IDL routine LWSCOADD[2] provided by the observatory.

The IRAF/PHOT task was used for the photometric data reduction. Apertures of radius 0.$''$96 (12 pix) were used for the photometry and the sky background was measured in 2.$''$0–3.$''$2-radius (25–40 pix) annuli. Flat-fielding was found to increase the scatter in the photometry and therefore not performed. A curve-of-growth correction of -0.12 $\pm$ 0.01 mag (based on standard star measurements) to a 1$''$.92 (24 pix) aperture was applied to each star, resulting in magnitudes within $\sim$5% of the infinite aperture value. Standard star observations were used to obtain extinction curves for each

[2] LWSCOADD is available at http://www.astro.caltech.edu/mirror/keck/inst/lws/lwscoadd_pro.html, provided by Gregory D. Wirth.

Table 5.2. Observations

Source	Date of Obs.	reference star	aperture	LSEC?	
49 Cet	Nov 8, 2000	α Tau	6	n	
HD 17925	Feb 21, 2000	HR 1017	6	y	
HD 22049	Dec 10, 2000	HR 1017	6	y	
IRAS 04295+2251B	Dec 9, 2000	HR 617	6	y	
AA Tau	Feb 21, 2000	HR 2990	6	y	
LkCa 15	Nov 30, 1999, Nov 8, 2000	α Aur [a]	6,3	n,n	
GM Aur	Nov 8, 2000	α Tau [a]	3	n	
MWC 480	Nov 30, 1999	α Tau	6	n	
HD 233517	Nov 8, 2000	α Aur	3	n	
Hen 3-600A	Feb 21, 2000	HR 4786	6	y	
HD 102647	Feb 19, 2000	HR 4534	6	y	
HR 4796A	Feb 21, 2000	HR 4786	6	y	
IRAS 14050-4109	Feb 21, 2000	HR 4786 [a]	6	y	
HD 163296	Aug 23, 1999,June 20, 2000	β Oph	6,3	n,y	
HD 179218	Feb 21, 2000	HR 5908	6	y	
WW Vul	June 20, 2000	ϵ Cyg [a]	3	y	*
HD 184761	Nov 8, 2000	α Tau	3	n	
HD 216803	Dec 9, 2000	HR 1017	6	y	
IRAS 04016+2610	Dec 9, 2000	HR 617	6	y	
IRAS 04248+2612	Dec 9, 2000	HR 617	6	y	
IRAS 04264+2433	Dec 9, 2000	HR 1017 [a]	6	y	
IRAS 04287+1801	Dec 9, 2000	HR 1708	6	y	
IRAS 04108+2803B	Dec 10, 2000	HR 1017 [a]	6	y	
IRAS 04181+2654A	Dec 10, 2000	HR 531 [a]	6	y	
IRAS 04181+2654B	Dec 10, 2000	HR 531 [a]	6	y	
IRAS 04381+2540	Dec 10, 2000	HR 531 [a]	6	y	
IRAS 04169+2702	Dec 10, 2000	HR 1017	6	y	
IRAS 04239+2436	Dec 10, 2000	HR 1017	6	y	
BNKL	Dec 10, 2000	HR 2943	6	y	
IRS2 NGC2024	Dec 10, 2000	HR 2943	6	y	
MonR22 IRS3	Dec 10, 2000	HR 2943	6	y	
IRAS 04489+3042	Feb 21, 2000	HR 1708[a]	6	y	
Haro 6-10A	Dec 10, 2000	HR 1017	6	y	
Haro 6-10B	Dec 10, 2000	HR 1017	6	y	

[a]Residuals of incomplete subtraction of the 9.7 μm telluric ozone feature are present in the spectrum.

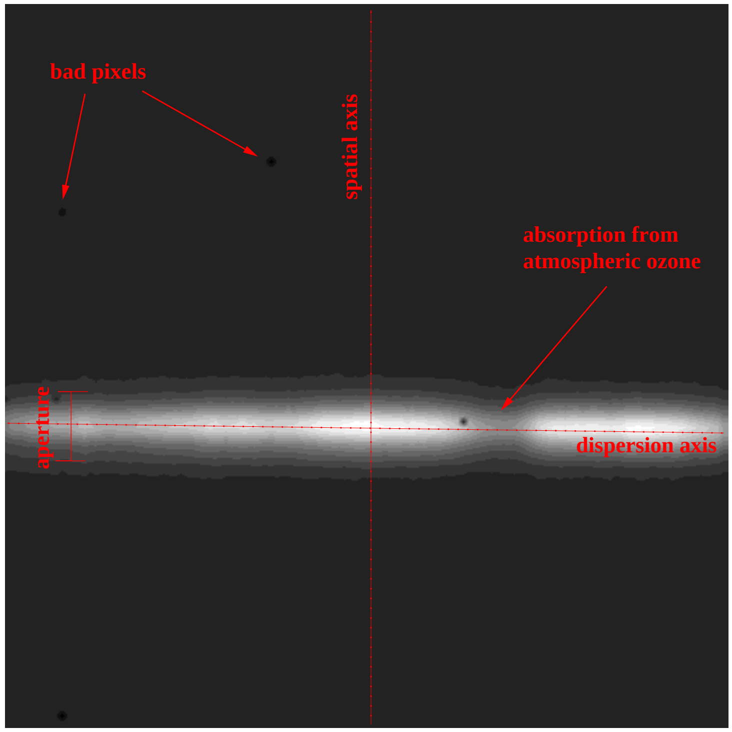

Figure 5.2 Coadded image of standard star HR 1165. Images were corrected for bad pixels, flat fielded and the slope in the dispersion axis is removed. The spectra were then summed along the spatial axis to obtain the final spectrum.

night, resulting in a typical night-to-night variation in the atmospheric zero-points of ∼20% and an average atmospheric extinction correction of -0.32 ± 0.07 mag/airmass. The root-mean-square scatter in the photometry of the standards is 0.06 mag for Feb 20 and 21, and 0.13 mag for Dec 9, 2000.

The spectroscopy data reduction was also performed using the NOAO IRAF/TWODSPEC and ONEDSPEC tasks. Bad pixel masks were composed from the flats and corrected in the source images. The images were flat fielded prior to extraction in order to calibrate for pixel-to-pixel variations across the detector. The images were then divided by those produced from the LSEC calibration scan obtained closest in time to the observation, to correct for variations in the spectral response of the grating. The detector's dark field flux was found to be negligible over the integration times used and therefore not subtracted from the data. Extraction of the spectra was performed using the *IRAF* task *apall*. In this task, a trace function is fit to the dispersion axes and used to correct the center of the apertures at each dispersion point in the image. The spectrum is then extracted from the image by summing over the selected aperture in the spatial direction.

The central wavelength on the detector varies slightly each time the grating and slit are moved, individual wavelength calibration is therefore required. For the purposes of wavelength calibration and removal of the telluric ozone absorption feature at ∼9.5 μm, each extracted spectrum was aligned with and divided by a standard star spectrum (see Table 5.2 for details) using the *telluric* task. In order to achieve the best match for each source-calibrator pair (lowest residual rms), the standard star spectrum was scaled and shifted to match the source spectrum before division. However, in some cases (as noted), variations in seeing resulted in small differences in the shape of the ozone feature in the stellar and calibrator spectra and residuals can be seen in the resulting spectra. Although the calibrators are chosen to possess a flat continuum in the 8–13 μm range, the resulting spectra were then multiplied by a blackbody emission spectrum for the calibrator to remove any slope present.

Finally, the spectra were flux calibrated using the photometric observations at similar wavelengths culled from the literature (see Table 5.3). Each spectrum was summed over the bandwidth used for the corresponding photometry and the result was scaled to match the photometric flux. This scaling factor was then applied to obtain the flux calibrated spectra shown in Figures 5.3-5.7. Overplotting the spectra onto the SEDs indicates the success of the flux calibration.

5.4 Spectral energy distributions (SEDs)

Previous observations of continuum fluxes for the sources in our sample were collected from the literature in order to form the Spectral Energy Distributions (SEDs) shown in Figures 5.3-5.7. The data were not de-reddened, but, as the A_V for these sources is small ($A_V < 3$), this should have very little effect on fluxes for wavelengths longer than K band. In order to determine the contribution from stellar radiation, the SEDs were fit with emission arising from a blackbody at the stellar temperature given in the literature for each source (see Table 5.1) by scaling the peak of the blackbody curve to match the SED at that wavelength. The flux from the stellar blackbody F_{bb} $[erg/cm^2/s/\mu m]$ is defined by the equation,

$$F_{bb} = \frac{2hc^2/\lambda^5}{e^{hc/\lambda kT} - 1} \frac{\pi R^2}{D^2}, \tag{5.6}$$

where h, c, and k have the usual definitions, λ is the wavelength in μm, R is the radius of the star and D is the distance to the star so that $\frac{\pi R^2}{D^2}$ is the solid angle subtended by the star. Stellar luminosities were found by integrating this blackbody flux over wavelength,

$$L_* = \int 4\pi D^2 F_{bb}\, d\lambda, \tag{5.7}$$

and are listed in Table 5.4. For comparison, stellar luminosities from the literature are also presented. These are similar to the luminosities derived here, but our estimates are consistently smaller than the luminosities from the literature, which is consistent with errors due to not dereddening the observed SED fluxes.

It is useful to compare the luminosity from circumstellar dust radiated in the millimeter and IR (L_{IR}) with the total luminosity from the source (L_{tot}). In previous studies of T Tauri stars,

Table 5.3. Flux calibration of spectra

Source	$\lambda(\mu m)$	Flux (Jy)	$\Delta\lambda$ (km/s)	Instrument	Ref.
49 Ceti	10.8	0.2 $\pm$0.04	8.0–13.6	KeckII,OSCIR	1
LkCa 15	9.6	0.5 $\pm$0.15	9.5–9.7	ISO,SWS	2
GM Aur	10.1	0.5 $\pm$ 0.0	7.55–12.65	IRTF	3
MWC 480	9.6	8.7 $\pm$ 2.6	9.5–9.7	ISO,SWS	2
HD 233517	10.1	0.439 $\pm$ 0.0	9.595–10.505	UKIRT,Berkcam	4
HD 163296	9.69	18.6 $\pm$ 0.5	8.84–10.54	1m,ESO	5
WW Vul	9.6	2.3 $\pm$ 0.5	9.5–9.7	ISO,SWS	2
HD 184761	12	2.41 $\pm$ 0.0	9.15–14.85	IRAS	6
HD 179218	10.7	17 $\pm$ 2	10.15–11.25	O'brien Obs.	7
HD 22049	12	9.5 $\pm$ 0.4	9.15–14.85	IRAS	6
BN	10.7	88 $\pm$ 0.0	10.0–11.4	Keck,LWS	8
HD 216803	10.7	1.53 $\pm$ 0.082	10.0–11.4	Keck,LWS	9
Hen 3-600A	10.7	0.73 $\pm$ 0.06	10.0–11.4	Keck,LWS	9
HD 102647	10.7	5.51 $\pm$ 0.41	10.0–11.4	Keck,LWS	9
HD 17925	10.7	0.92 $\pm$ 0.09	10.0–11.4	Keck,LWS	9
AA Tau	10.7	0.44 $\pm$ 0.03	10.0–11.4	Keck,LWS	9
HR 4796A	10.7	0.216 $\pm$ 0.02	10.0–11.4	Keck,LWS	9
IRAS 04016+2610	10.7	2.84 $\pm$ 0.18	10.0–11.4	Keck,LWS	8
IRAS 04016+2610	10.3	2.5 $\pm$ 0.0	9.65–10.95	IRTF	10
IRAS 04108+2803B	10.7	0.68 $\pm$ 3.0	10.0–11.4	Keck,LWS	8
IRAS 04108+2803B	10.3	0.57 $\pm$ 0.0	9.65–10.95	IRTF	10
IRAS 04248+2612	10.7	0.23 $\pm$ 0.009	10.0–11.4	Keck,LWS	8
IRAS 04264+2433	10.7	0.41 $\pm$ 0.02	10.0–11.4	Keck,LWS	8
IRAS 04287+1801	10.7	5.02 $\pm$ 0.4	10.0–11.4	Keck,LWS	8
IRAS 04295+2251B	10.7	0.69 $\pm$ 0.03	10.0–11.4	Keck,LWS	8
IRAS 04489+3042	10.7	0.31 $\pm$ 0.02	10.0–11.4	Keck,LWS	8
IRAS 14050-4109	10.7	0.234 $\pm$ 0.022	10.0–11.4	Keck,LWS	9
IRAS 04181+2654A	12.0	0.358 $\pm$ 0.0	9.15–14.85	IRAS	6
IRAS 04181+2654B	12.0	0.358 $\pm$ 0.0	9.15–14.85	IRAS	6
IRAS 04239+2436	12.0	1.712 $\pm$ 0.0	9.15–14.85	IRAS	6
IRAS 04381+2540	10.6	0.209 $\pm$ 0.0	10.5–10.7	...	...
IRAS 04239+2436	12.0	1.71 $\pm$ 0.086	9.15–14.85	IRAS	6

Note. — References: 1-Jayawardhana et al. (2001), 2-Thi et al. (2001), 3-Kenyon & Hartmann (1995), 4-Skinner et al. (1995), 5-Berrilli et al. (1992), 6-Beichman et al. (1988), 7-Lawrence et al. (1990), 8-Hillenbrand, private communication, 9-Metchev et al. (2003), 10-Myers et al. (1987)

Table 5.4. Calculations from SEDs: Class II, III objects

Source	λ_{onset} (μm)	L_*-lit ($L_\odot$)	L_* ($L_\odot$)	L_{IR} ($L_\odot$)	L_{tot} ($L_\odot$)	L_{IR}/L_{tot} ($L_\odot$)	L_{IR}/L_* ($L_\odot$)
LkCa 15	1.65	0.97	0.344	0.452	0.796	0.568	1.31
GM Aur	6.9	0.84	0.697	0.327	1.02	0.319	0.469
MWC 480	2.2	23.7	15.4	3.31	18.7	0.177	0.215
HD 163296	1.4	35.2	25.3	8.41	33.7	0.249	0.332
WW Vul	1.4	43.0	25.6	15.7	41.3	0.380	0.613
HD 184761	2.3	...	9.14	0.641	9.78	6.55e-2	7.01e-2
AA Tau	1.9	0.71	0.221	0.593	0.814	0.729	2.68
HD 179218	0.91	221.9	75.3	35.0	110	0.317	0.465
IRAS 14050-4109	1.5	...	0.440	4.28e-2[a]	0.483	8.86e-2	9.73e-2
Hen 3-600A	5.4	0.23	0.202	-4.52e-2[b]	0.247	<0.183	<0.224
49 Ceti	11.3	23.44	19.5	1.69e-2	19.5	8.66e-4	8.70e-4
HD 233517	6.3	0.20	0.341	1.56e-2	0.356	4.37e-2	4.57e-2
HR 4796A	12.4	35.0	30.7	6.24e-2	30.8	2.03e-3	2.00e-3
HD 22049	100	...	0.364	-2.44e-2[b]	0.340	<6.28e-2	<6.70e-2
HD 216803	20	...	0.209	5.11e-5	0.209	2.44e-4	2.44e-4
HD 102647	60	...	19.0	-3.51e-3[b]	19.0	<1.85e-4	<1.85e-4
HD 17925	60	...	0.368	9.66e-3	0.378	2.56e-2	2.62e-2

[a]This is a lower limit. Had to cut off luminosity estimate at the last observed point (100μm) due to bad fit.

[b]Small IR excesses led to the calculation of negative values for L_{IR}. The absolute values of L_{IR} are used for calculations of upper limits to L_{IR}/L_{tot} and L_{IR}/L_*.

Table 5.5. Calculations from SEDs: Class I objects

Source	RA(J2000))	DEC(J2000)	L_{tot}[c]	Ref.
IRAS 04016+2610	04 04 42.85	+26 18 56.3	3.74	1,3
IRAS 04108+2803B	04 13 52.9	+28 11 23	0.344	1,3
IRAS 04181+2654	04 21 11.42	+27 01 08.9	0.406	1,2,3
IRAS 04239+2436	04 26 57.1	+24 43 36	0.394	1,3
IRAS 04248+2612	04 27 56.7	+26 19 20	22.8	1,3
IRAS 04264+2433	04 29 07.68	+24 43 50.1	0.244	1,3
IRAS 04287+1801	04 31 33.6	+18 08 15	0.292	1,3
IRAS 04295+2251B	04 32 32.07	+22 57 30.3	1.43	1,2,3
IRAS 04325+2402	04 35 33.0	+24 08 14	0.717	1,3
IRAS 04381+2540	04 41 12.48	+25 46 37.1	0.350	1,2
IRAS 04489+3042	04 52 06.9	+30 47 17	0.350	1,3
BN object	05 35 14.17	-05 22 23.1	114	...
NGC 2024 IRS2	05 41 45.8	-01 54 30	...	...
MonR2 IRS3	06 07 47.8	-06 22 55	...	...

[c]Assumed a distance of 140 pc for embedded sources in the Taurus molecular cloud. As the spectral types and A_V's are unknown, no stellar blackbody was fit and SED fits give L_{tot}.

Note. — References: 2-Hartmann,2002ApJ...578..914H - Astrophys. J., 578, 914-924 (2002) - October(III) 2002, 3-IRAS Faint Source Catalogue version 2 (1990) the fractional luminosity (L_{IR}/L_{tot}) has been measured (using IRAS measurements to calculate L_{IR}) and was found to clearly distinguish between the standard classes (Kenyon & Hartmann, 1987); $L_{IR}/L_{tot} > 0.8$ for class I sources (embedded stars), $L_{IR}/L_{tot} \approx 0.1$–$0.2$ for class II sources (optically thick disks), and $L_{IR}/L_{tot} < 0.1$ for class III sources (optically thin disks). Another important quantity is the ratio of the IR to stellar luminosity (L_{IR}/L_*), which is related to the optical depth of the disk material. For optically thin emission, this luminosity ratio is indicative of the disk geometry as L_{IR}/L_* indicates the optical depth along the midplane for a geometrically thin disk (Backman & Paresce, 1993). The maximum value of L_{IR}/L_* is 1/4 for a flat optically thick disk and L_{IR}/L_* may reach 1/2 for a flared, optically thick disk, in which the thickness increases with distance from the star. Vega-like stars have $L_{IR}/L_* \sim 10^{-5}$–10^{-3} indicating low optical depths at all wavelengths (Sylvester et al., 1996).

The IR luminosity and the ratios L_{IR}/L_* and L_{IR}/L_* were thus estimated from the SEDs collected for our sample in the following manner. First, a polynomial was fitted to the points in the SED and through careful examination the wavelength λ_{onset}, at which this fit and the stellar blackbody diverge, was evaluated. The infrared luminosity of the disk L_{IR} was then calculated by integrating over the fit beyond λ_{onset} ($\lambda = \lambda_{onset} - 1$ cm) and subtracting the integral of the stellar blackbody over the same region. The total luminosities ($L_{tot} = L_{IR} + L_*$) and the resulting fractional IR luminosities L_{IR}/L_{tot} and IR-to-stellar luminosity ratios L_{IR}/L_*, as well as the wavelength of the onset of disk radiation, are presented in Tables 5.4–5.5.

The L_{IR}/L_{tot} classification of Kenyon & Hartmann (1987) appears to be consistent with our sample and applicable to both low and intermediate mass stars; the debris disks possess $L_{IR}/L_{tot} < 0.1$ and the optically thick protoplanetary disks possess $L_{IR}/L_{tot} > 0.1$–0.7. Additionally, λ_{onset} appears to be in general inversely proportional to the IR excess, and the debris disks are easily identified as those sources with large λ_{onset} and low fractional IR luminosities. For the younger sources, we find very high values of L_{IR}/L_*, always greater than 0.3 with a maximum at 2.68 for AA Tau, similar to the range that was found for a large sample of TTs by Cohen et al. (1989). This cannot be explained by passive thermal reprocessing of radiation by grains and according to the classification of Sylvester et al. (1996) a flared disk geometry combined with energy release due to accretion is a possible explanation of these high IR excesses.

For the class I sources the stellar parameters are unknown and therefore only total luminosities were calculated. In the early stages of star formation, the total, or bolometric, luminosity should be approximately equal to the accretion luminosity (Kenyon & Hartmann, 1995),

$$L_{tot} = L_{acc} = \frac{GM_*\dot{M}}{R_*} \tag{5.8}$$

$$\approx 15 \left(\frac{M_*}{0.4M_\odot}\right) \left(\frac{R_*}{2.7R_\odot}\right)^{-1} \left(\frac{\dot{M}}{3\times10^{-6}M_\odot/yr}\right) L_\odot \tag{5.9}$$

$$\approx \quad 10 - 50\ L_{\odot}. \tag{5.10}$$

Most of the class I objects in our sample, however, possess $L_{tot} < 1\ L_{\odot}$, similar to what is seen by Kenyon & Hartmann (1995) for a sample of low mass embedded stars. They suggest that this is due to an increased accretion radius or intermittent accretion onto the central star, but these scenarios cannot fully explain the extremely low luminosities observed for a large number of sources.

The SEDs are additionally useful for establishing a continuum around the 8–13 μm silicate emission feature, which is extremely important for analysis of the feature shape and the silicate composition. van Boekel et al. (2003) fit the SED with a blackbody for the star and several blackbodies of different temperatures for the dust emission and interpolate between the two to find the continuum. Natta et al. (2000) fit a powerlaw to the edges of the silicate emission feature to remove the continuum. Upon examination of the overlays of the spectra on the SEDs in Figure 5.4-5.5, we find that the continuum is in most cases adequately represented by connecting the two endpoints of the spectrum (at approximately 8.3 and 12.2 μm). The one exception is the T Tauri star AA Tau for which the SED contains photometry with large flux variations near 10 μm and the continuum is difficult to establish. In this case, a flat continuum with flux equal to the flux at the 8 μm end of the spectrum was used.

In general, we would expect the shape of the feature to be related to the SED and the amount of radiation from the star versus the disk. Specifically, if the changes in the silicate feature are due to processing of the dust, and conversion of the dust composition from primarily amorphous olivines to crystalline enstatite and forsterite, then this should be related to the evolutionary stage of the disk. As described above, the fractional IR luminosity is another indicator of the evolutionary class and thus we would expect that objects with lower L_{IR}/L_{tot} values in any class would be more likely to have flatter 8–13 μm spectra, with more emission from the 11.2 μm crystalline silicate feature.

5.5 10 μm spectra

The flux calibrated spectra and SEDs are shown in Figures 5.3-5.7 and continuum subtracted spectra are shown in Figure 5.8. The sources may be placed into categories based on the shape of the SEDs and 8–13 μm spectra. In general, the debris disks (more evolved than class III primordial disks) were found to have little or no evidence of silicate emission, the class II sources showed strong to moderate silicate emission and the class I sources showed silicate absorption, except for IRAS 04489+3042, IRAS 04108+2803B and IRAS 04264+2433, which show no feature. Possible evolutionary trends are shown in Figures 5.9 and 5.10 for the low mass and intermediate mass stars, respectively. The trend shown in Figure 5.10 is similar to that suggested for HAEBE stars by Meeus et al. (2001). The evolution of low mass star spectra and SEDs does not appear to be that different from intermediate

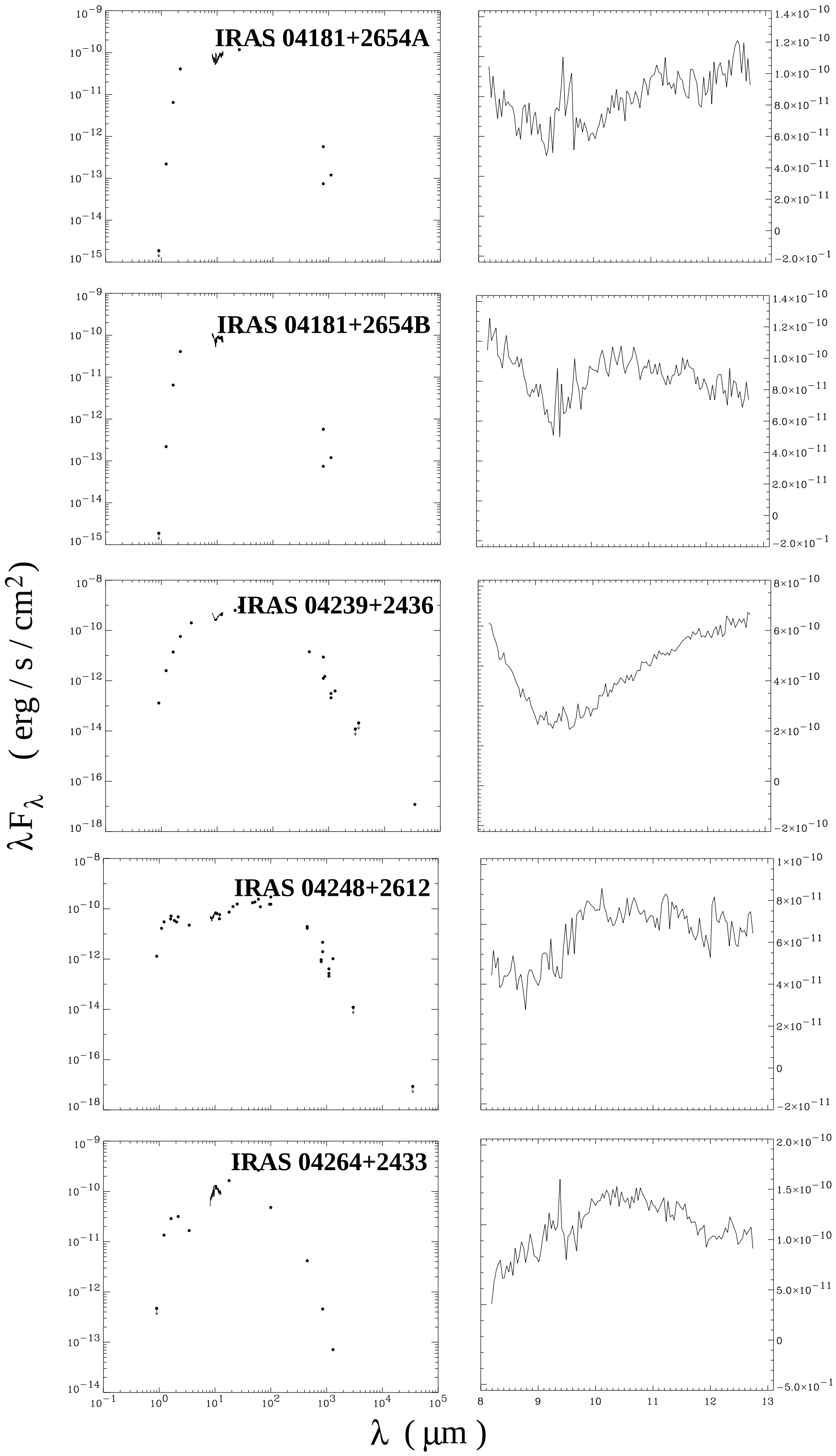

Figure 5.3 SEDs and 10 μm spectra for low mass star disks where silicates are in absorption or not detected. SEDs are plotted on a log scale while the spectra are presented on a linear scale.

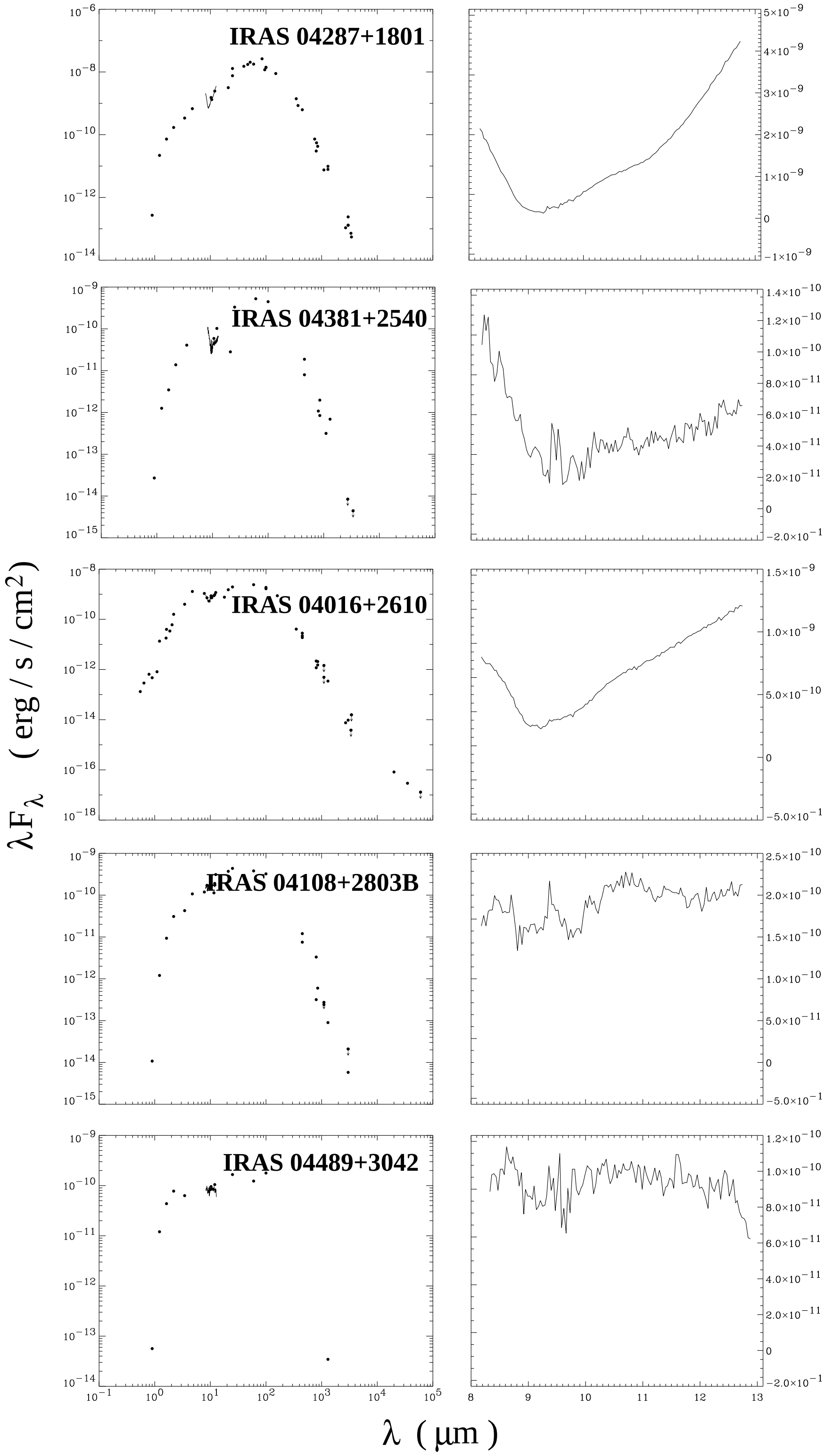

Figure 5.3 -continued

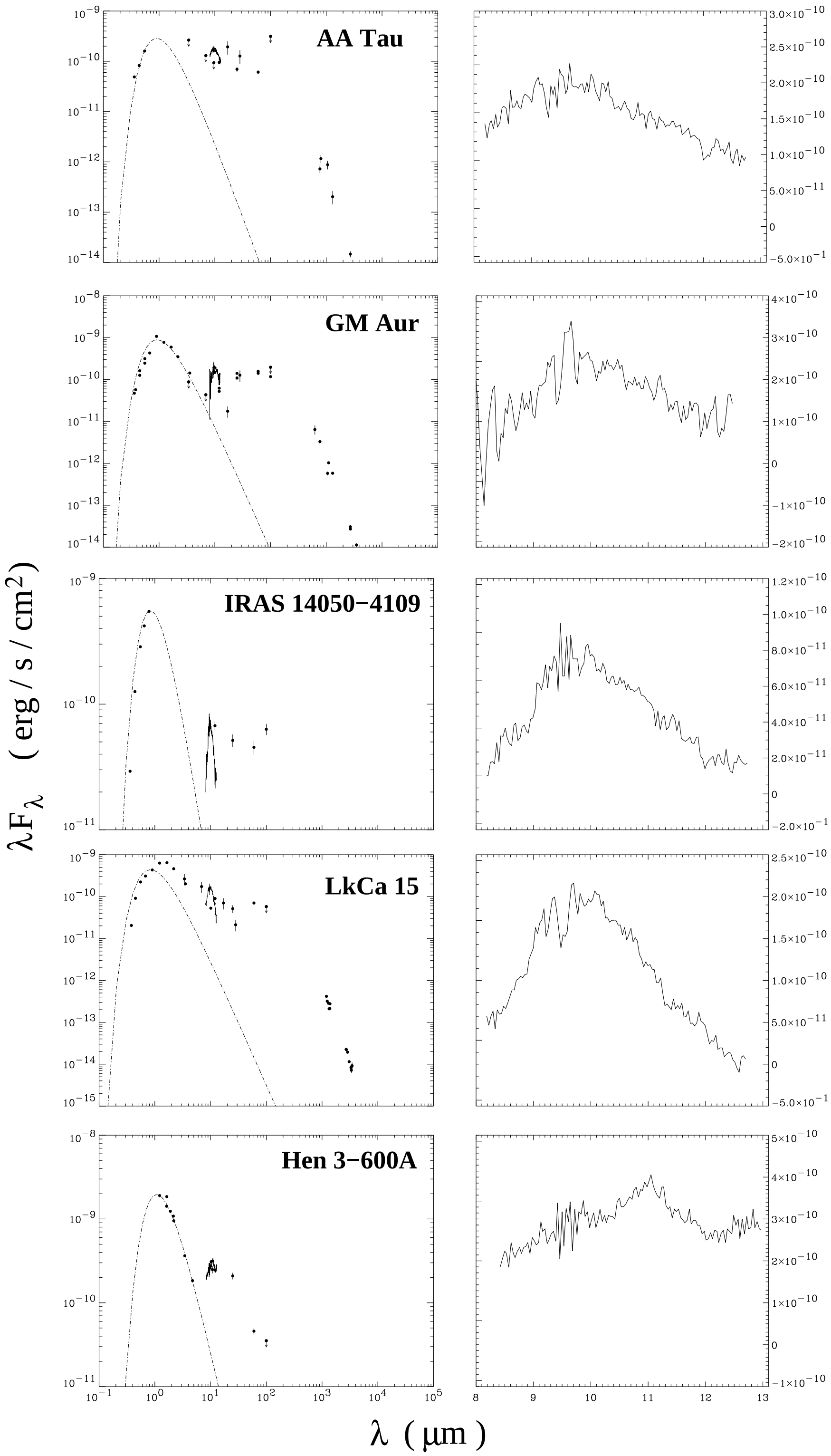

Figure 5.4 SEDs and 10 μm spectra for disks around low mass, T Tauri stars where the silicate 10 μm band is in emission.

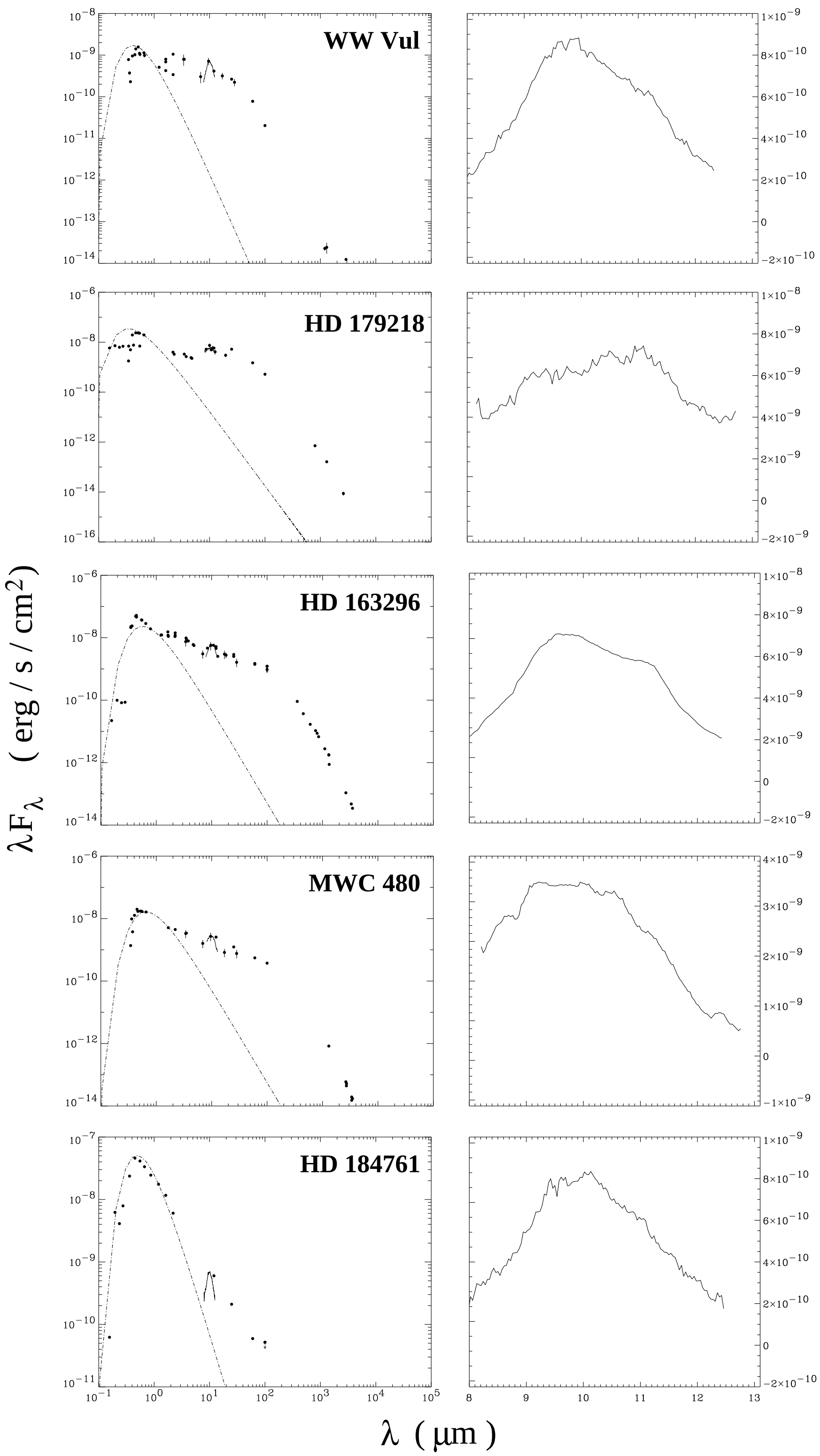

Figure 5.5 SEDs and 10 μm spectra for disks around intermediate mass, HAEBE stars where the silicate 10 μm band is in emission.

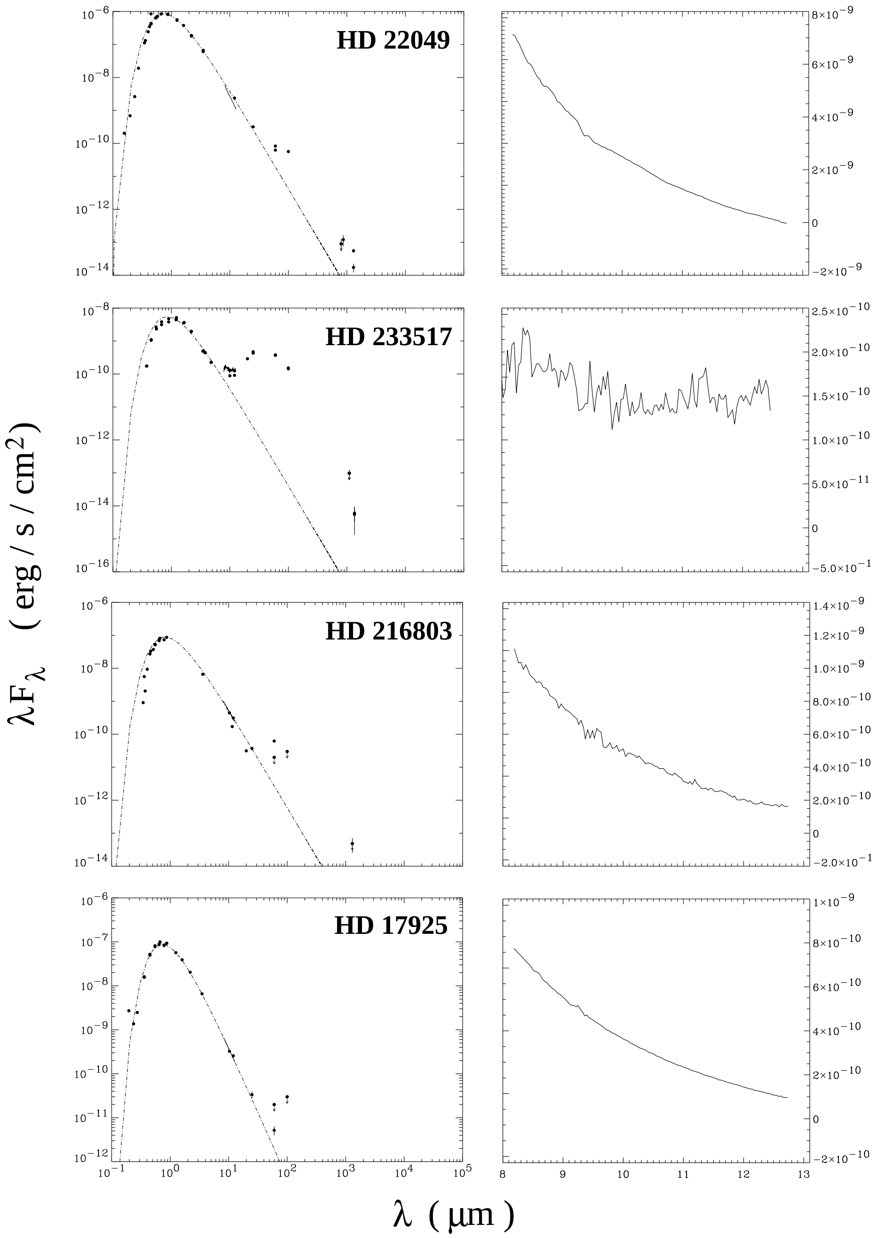

Figure 5.6 SEDs and 10 μm spectra for “debris” disks around low mass stars.

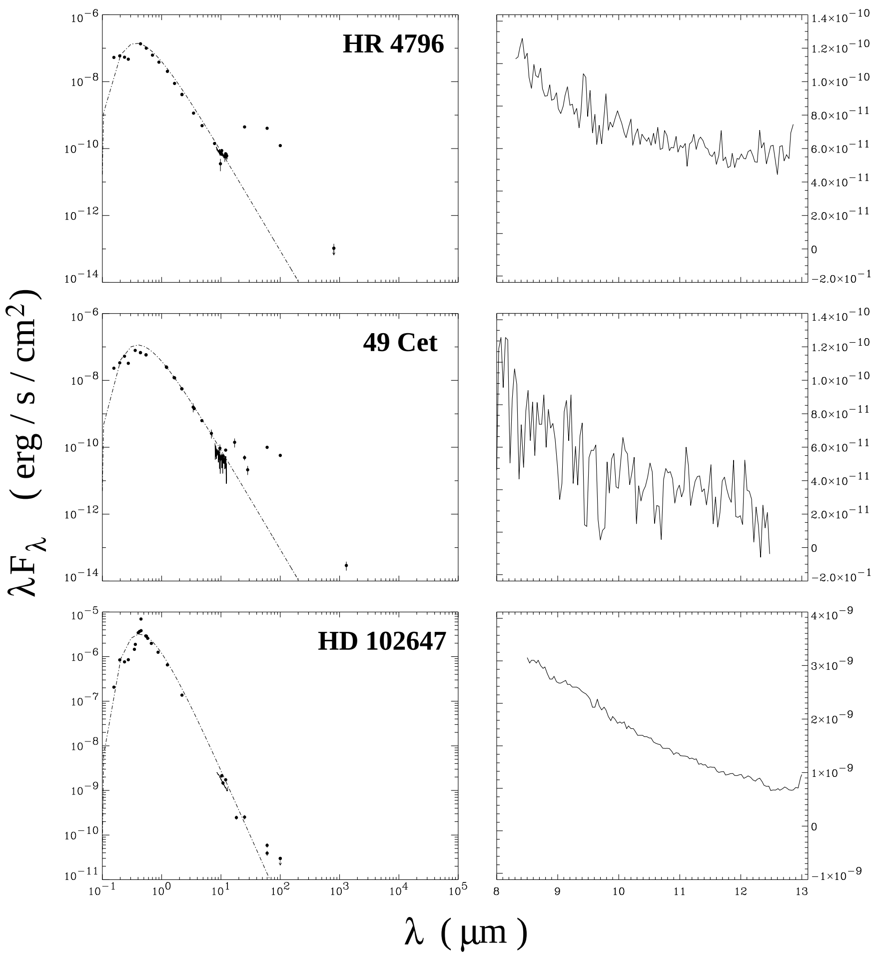

Figure 5.7 SEDs and 10 μm spectra for “debris” disks around intermediate mass stars.

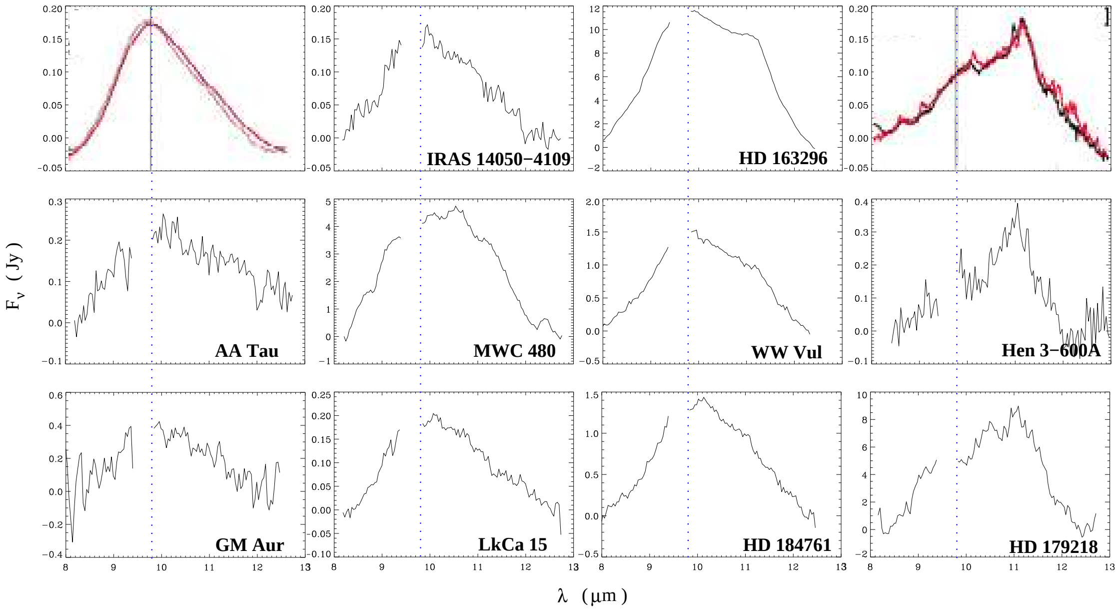

Figure 5.8 Continuum subtracted emission spectra, constructed via the method outlined in the text. Format is similar to Bouwman et al. (2001). The panels in the top left and top right are ISO spectra from Bouwman et al. (2001) of the amorphous olivines in the galactic center and the highly processed, crystalline forsterite-rich spectrum of HD 100546. The vertical dashed line indicates the position of the peak of the amorphous silicate band as observed for the ISM at 9.8 μm.

mass stars, with embedded sources showing amorphous olivine in absorption, followed by stages of dust processing (and possibly grain growth) leading to the observation of emission from crystalline forsterite and finally photospheric spectra for debris disks. One significant difference between the low and intermediate mass cases is that for intermediate mass stars, crystalline silicates have been found in sources which possess large FIR excesses, but for low mass stars, the only source in which crystalline silicates have been found is on the verge of being a debris disk.

The spectra observed toward the T Tauri stars GM Aur, AA Tau, IRAS 14050-4109 and LkCa 15 and the Herbig Ae star MWC 480 are similar to that of amorphous olivine. Although no crystalline features are evident, the spectra are wider in comparison to that of the Galactic center, suggesting that some processing has taken place in the disk. The absence of a strong crystalline component in the emission spectra indicates that this processing is more likely related to grain growth (discussed below) than to crystallization.

The spectra that we observed toward the HAeBe stars HD 163296, HD 184761, and WW Vul, each depict an emission feature characteristic of amorphous olivine and a secondary peak at 11.3 μm, perhaps due to a small amount of crystalline forsterite (much less than that seen for β Pictoris or HD 100546 (Meeus et al., 2001). These objects are all intermediate mass stars ($\sim$2 $M_\odot$) of ages > 6 Myr, and all three still possess considerable amounts of silicates, as can be seen by comparison of the silicate flux to that due to the stellar photospheres. This may indicate that dust crystallization is

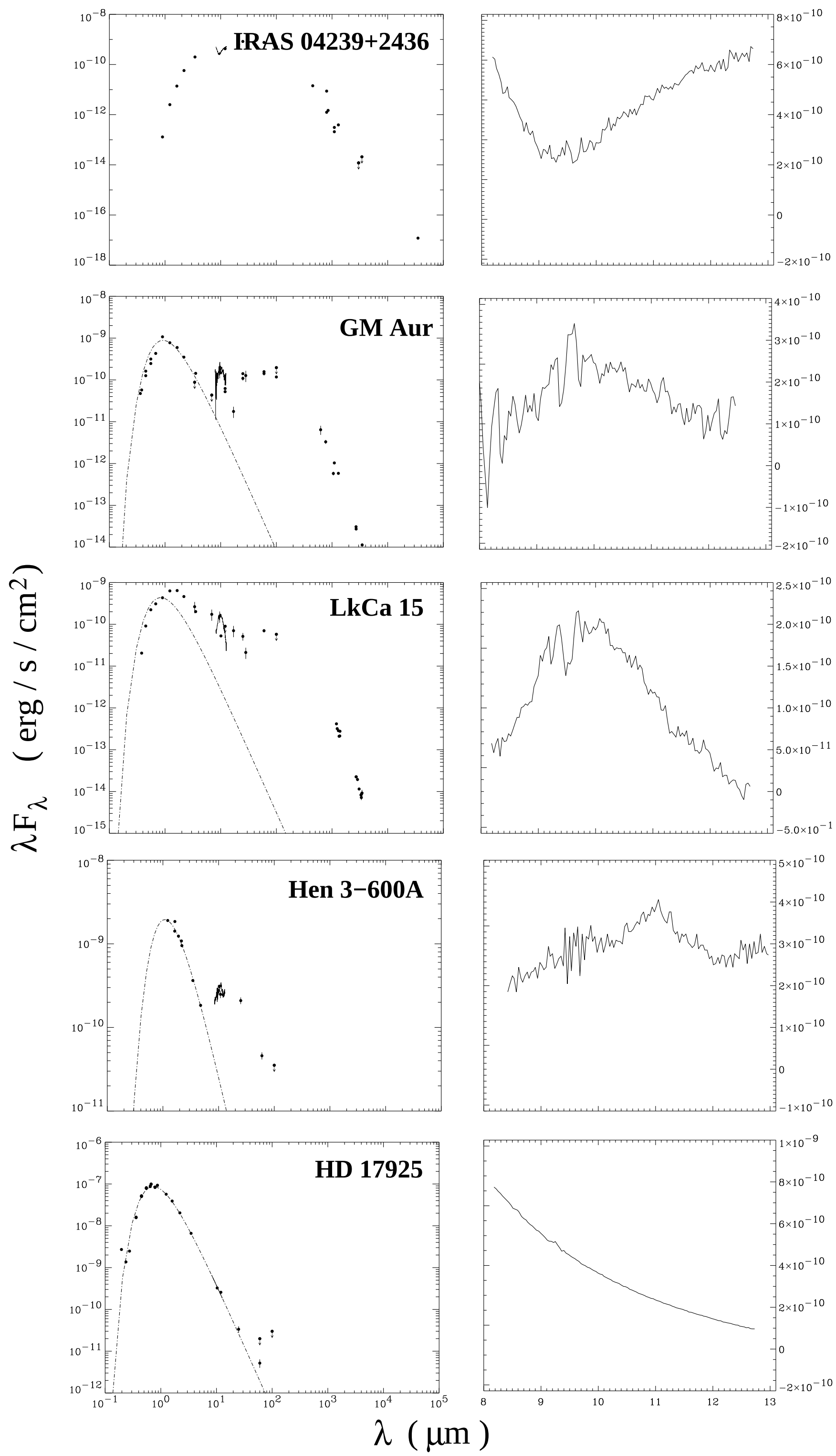

Figure 5.9 Evolution of the silicate spectrum for low mass stars. The evolutionary sequence for low mass stars is quite similar to that for intermediate mass stars (Meeus & Waelkens, 1999).

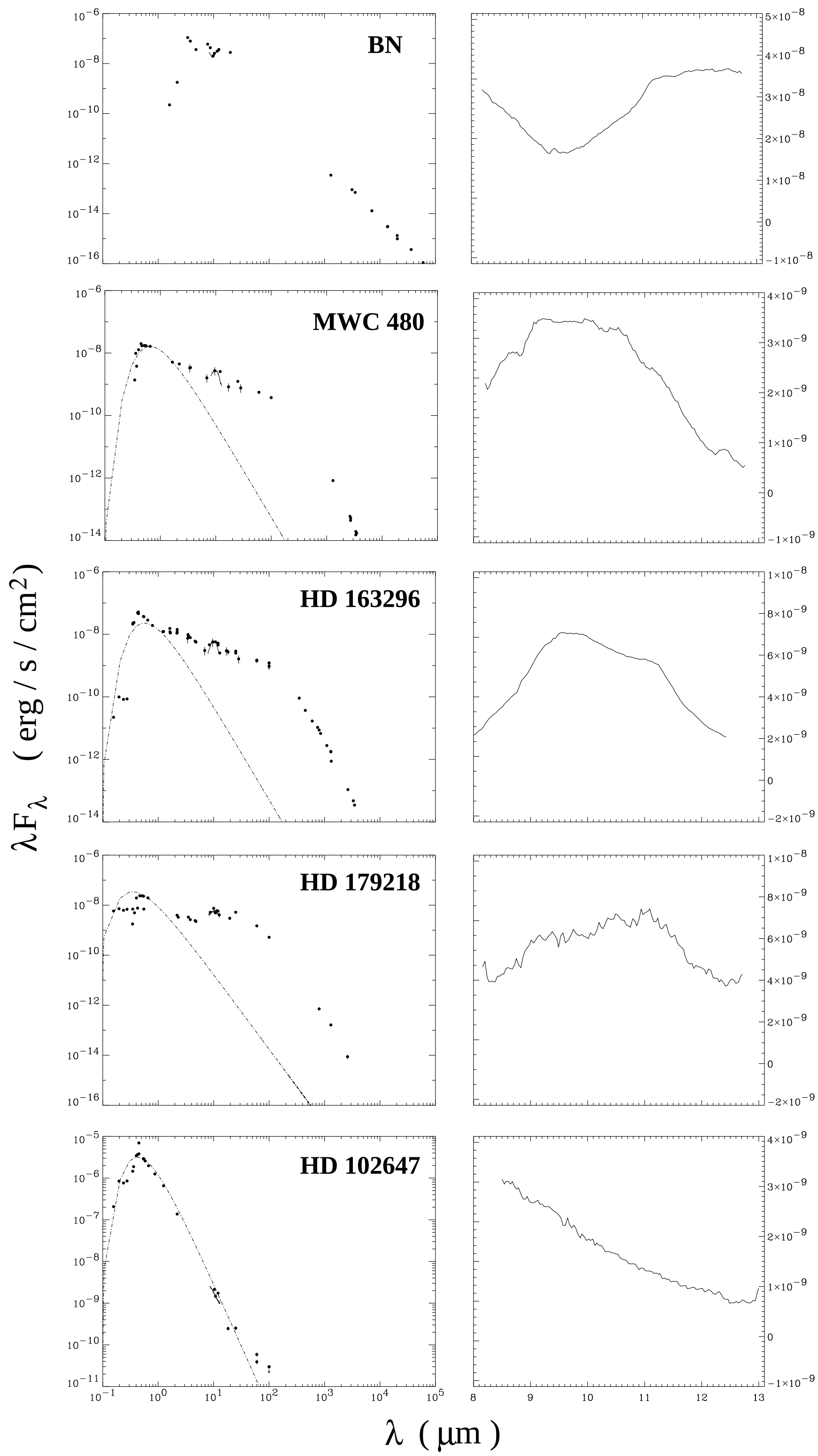

Figure 5.10 Evolution of the silicate spectrum for intermediate mass stars. The evolutionary sequence is similar to that observed for intermediate mass stars in ISO studies (Meeus & Waelkens, 1999).

not directly related to the processes involved in dust clearing. The spectra of the latter two objects are similar to that observed toward a few objects by Hanner et al. (1995), which are fit with models that include the emission from both silicates and poly-aromatic hydrocarbons (PAHs).

Perhaps the most interesting result is the similarity between the silicate emission from the low mass star Hen 3-600A and the Herbig Ae star HD 179218 (also similar to the HAEBE star HD 100546; Bouwman et al., 2003). Both show strong peaks at 11.3 μm, which dominate the spectrum. The shape of the emission feature is consistent with that of crystalline enstatite (including the correlating small peak at 10.2 μm). Hen 3-600A is the first low mass object to show emission from crystalline silicates. For these silicates to be detectable, they must be present at radii < 1 AU (T$\approx$200–300 K). In contrast, the warm silicates in the HAEBE star HD 179218 are likely to reside at a much larger distance from the star (R$\sim$10 AU). This observation, along with the presence of crystalline silicates in long period comets and cold crystalline silicates in HAEBE stars, suggests that crystalline silicates must either have a cold formation mechanism or be transferred outward. However, the presence of equivalent fractions of crystalline silicates around an HAEBE star which still possesses strong IR emission, and thus a substantial amount of warm dust as around a T Tauri star with much less IR flux and warm dust, may indicate that the process of crystallization takes longer around low-mass stars, which is consistent with the thermal annealing scenario.

No warm silicate emission was seen toward the debris disks–their spectra are entirely photospheric. A possible exception is HD 233517, which may possess Poly-Aromatic Hydrocarbons (PAHs–with features at 8.3, 9.7 and 11.2 μm) in addition to some silicates, but if so, these features are weak. The lack of silicate emission may indicate either a paucity of small grains (a < 10 μm), possibly due to grain growth, or the absence of a significant amount of optically thin material inside of $\sim$10 AU (T$\geq$200 K). The absence of a substantial continuum at 10 μm is consistent with the SEDs for HD 102647, HD 17925, HD 22049 and HD 216803, which show very low IR and millimeter excesses ($L_{IR}/L_{tot} \sim 0.001$) with $\lambda_{onset} \geq 60$ μm. This suggests that the debris disks have lost most of their (warm, small) circumstellar silicate grains. 49 Ceti, HR 4796A and HD 233517, however, still possess substantial far-IR and millimeter excesses. The presence of dips in the SED around 10 μm and the absence of silicate emission suggest the presence of large gaps in the disk at radii close to the star, similar to that proposed for the T Tauri star GM Aur (Rice et al., 2003).

5.5.1 Variability

Multiple spectra were obtained toward a few sources allowing determinations of the variability of the shape and strength of the silicate emission to be evaluated. Figure 5.11 shows the silicate emission toward HD 163296 and LkCa 15 for two observations, taken approximately one year apart. Spectra from the two observing runs are overlaid, showing that there is no significant variability (above the error) in the shape of the silicate emission feature for these two sources on a yearly timescale. The double peaked structure seen in the spectrum of HD 163296 has been previously observed in spectra obtained by ISO (Bouwman et al., 2001; October, 14 1996) and ground-based observations (Sitko et al., 1999; October, 10 1996) and the shape of the spectra observed does not differ significantly from our observations.

The silicate emission from HD 179218, MWC 480 and Hen 3-600A have also been previously observed by Bouwman et al. (2001) (ISO LWS; Oct 5, 1996), Sitko et al. (1999) (IRTF BAAS; Oct 14, 1996) and Honda et al. (2003) (Subaru COMICS; Dec 27, 2001), respectively. The previous observations of HD 179218 (Bouwman et al., 2001) are virtually identical to our observations (Feb 21, 2000); they depict very similar peak strengths ($\sim$9 Jy, when taking the continuum level at 8.0 μm) and shapes (the slope is approximately the same, the peak lies near 11.3 μm and evidence of small peak at 8.0 μm is seen in both cases). MWC 480, however, exhibits very different emission in the Sitko et al. (1999) study than in our spectrum (Nov 30, 1999); in particular, the 11.3 μm feature (crystalline forsterite) is much less prominent in our observations and there is an additional peak at $\sim$10.5 μm (near the position of crystalline enstatite). However, the (peak-to-continuum) strength of the feature is the same to within $\sim$15%. The observations of Hen 3-600A by Honda et al. (2003) also suggest strong evidence of variability when compared to our data (Figure 5.11; Feb 21, 2000), in this case on shorter timescales ($\sim$ 1 yr). The LWS spectrum taken in 2000 shows much less emission at 9.2 μm and possibly 10.3 μm (both attributed to enstatite), with the peak at 11.3 μm (forsterite) dominating the spectrum. There also appears to be an accompanying decrease in the continuum or in the strength of emission near 12.5 μm from 2000 to 2001.

There is no obvious trend in the variability with respect to spectral type or silicate emission feature shape from these observations. HD 179218 and Hen 3-600A have similar emission features and yet the spectrum of Hen 3-600A is highly variable on 1 yr timescales while the spectrum of HD 179218 appears to have not changed in >3 yr. Although HD 163296 and MWC 480 possessed similar spectra in 1996 (Sitko et al., 1999), the spectra for these sources are quite different from each other in 1999 (our data); HD 163296 appears to be constant, while MWC 480 has undergone changes in the spectrum which appear to indicate conversion between the crystalline forms of forsterite (Mg_2SiO_4) and enstatite ($MgSiO_3$). This is similar to changes in the Hen 3-600A spectrum, which also appear to indicate decreasing emission from forsterite and increasing emission from enstatite, which is the opposite of the expected transition with time during the standard annealing process (see Gail (1998) and above discussion).

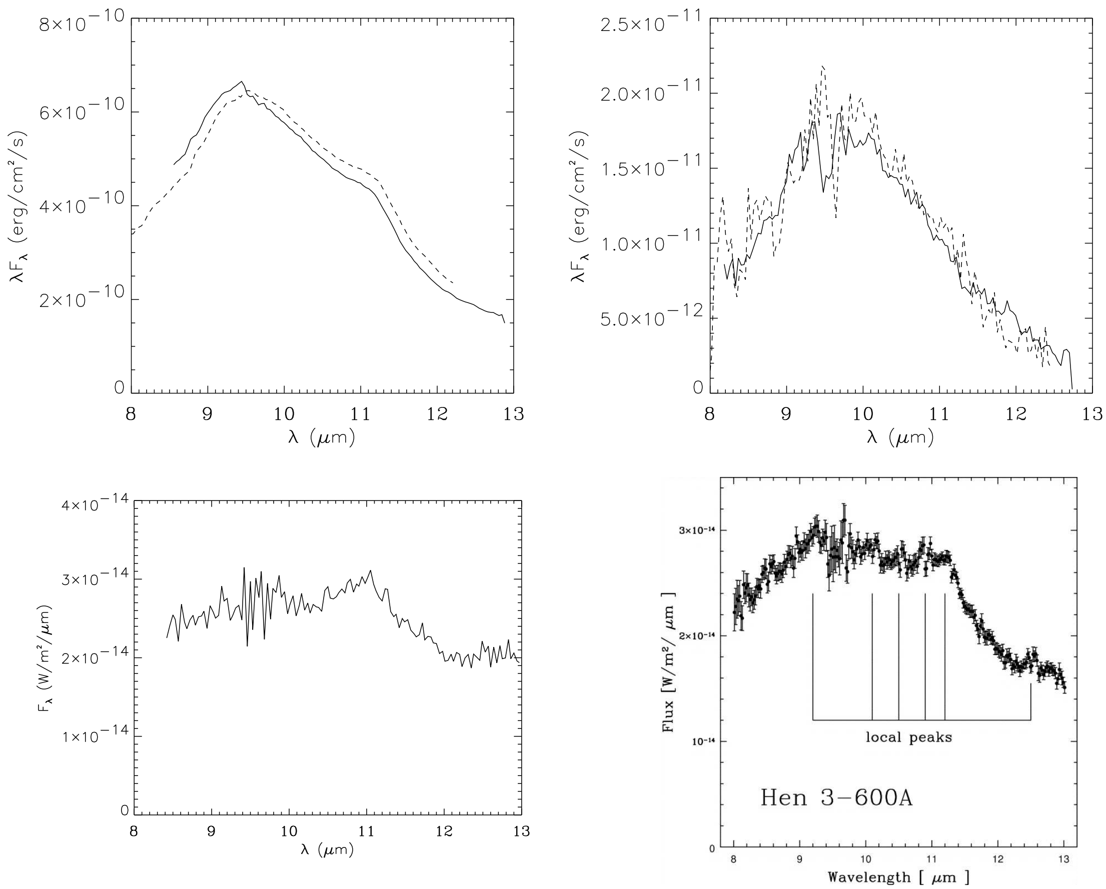

Figure 5.11 Searches for variability. The left panel shows the silicate emission toward HD 163296 observed on Aug 23, 1999 (solid line) and June 20, 2000 (dashed line). The right panel shows the silicate emission observed toward LkCa 15 on Nov 30, 1999 (solid line) and Nov 8, 2000 (dashed line). The spectra from two observing runs are overlaid, showing that there is no significant variability (above the error) in the shape of the silicate emission feature for these two sources on a yearly timescale. The bottom panel shows the Hen 3-600A spectrum in the same units as displayed in Figure 1 of Honda et al. (2003) indicating significant differences in the shape of the spectrum. The continuum was not subtracted for any of these spectra.

5.6 The silicate dust sequence: Dust composition and disk morphology

Having presented our spectra and discussed their overall properties qualitatively, we now embark on a quantitative description of the emission spectra. Sloan & Price (1995, 1998) find that the shape of 10 μm emission from oxygen-rich dust shells around several thousand late type AGB stars (after removal of the stellar continuum with an Engelke function) evolves from sharp emission peaking at 9 μm to broad emission which peaks at $\lambda > 11$ μm. The stars are then classified by the ratios of the flux from the dust shell at 10, 11 and 12 μm and a relationship between the width of the feature, indicated by F_{10}/F_{11}, and the long wavelength shoulder, indicated by F_{10}/F_{12}, was found:

$$F_{10}/F_{12} = 1.32(F_{10}/F_{11})^{1.77}, \tag{5.11}$$

which they called the *silicate dust sequence*. They further define a silicate emission index,

$$n = 10(F_{11}/F_{12}) - 7.5, \tag{5.12}$$

which evolves from SE8 ($n = 8$) for narrow emission centered near 10 μm to broad, structured silicate emission (SE1).

Egan & Sloan (2001) searched for a physical basis for the silicate dust sequence through examination of the dependence of the index on the temperature distribution, optical depth, geometric thickness and chemical composition of the dust shell through radiative transfer models using Mie theory with spherical grains. They find that grain size and shape (fractal versus spherical) only have a slight effect on the shape of the 10 μm silicate emission feature. These models also show that variations in geometric thickness of the dust shell have much smaller effects on the spectral (SE) index than variations in the inner shell radius. However, variations in the geometric thickness do have a large impact on the IR colors (IRAS) and therefore Egan & Sloan (2001) try to match the colors of the observed sequence as well as the SE index. They find that the smooth narrow emission features arise from optically thin shells of amorphous silicate dust and the broad, weak emission arises from optically and geometrically thin shells of alumina dust. For structured spectra in the middle of the silicate dust sequence, they find that more even mixtures of amorphous silicate and alumina *cannot* reproduce the observed spectra and IR colors and the shoulder at 11 μm can only be reproduced by optically thick, but geometrically thin shells of amorphous silicates. Increasing the optical depth of the shell drives the feature into self absorption, decreasing the contribution at 10 μm. The shell must be geometrically thin to match the IRAS colors.

As the composition of dust in protoplanetary disks is expected to be somewhat similar to oxygen

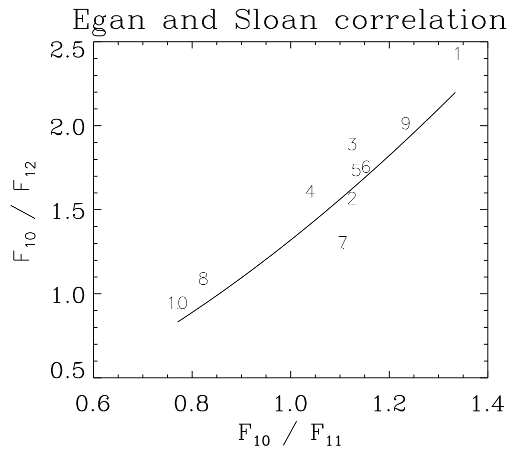

Figure 5.12 Plot of the slope of the feature width (F_{10}/F_{12}) to the slope of the high-wavelength side of the spectrum (F_{10}/F_{11}). The numbers correspond to: 1-LkCa 15, 2-GM Aur, 3-MWC 480, 4-HD 163296, 5-WW Vul, 6-HD 184761, 7-AA Tau, 8-HD 179218, 9-IRAS 14050-4109, 10-Hen 3-600A.

rich dust around AGB stars, although the geometrical distribution of the emitting dust is different, we have examined the applicability of the silicate dust sequence to the circumstellar disks in our sample. As in Egan & Sloan (2001), F_{10}, F_{11}, F_{12} are calculated from regions of ±0.2 around these central wavelengths. Also following Egan & Sloan (2001), the photospheric flux was divided out, but this has virtually no effect on the shape of our spectra because of the large IR excesses of disks as compared to AGB star continuum. As is shown in Figure 5.12 and Table 5.6, the F_{10}/F_{12} versus F_{10}/F_{11} for our disks are fit nicely by the silicate dust sequence. All of our sources lie at SE > 5, which, based on the interpretation of Egan & Sloan (2001), indicates that they are composed primarily of silicates (>80%), as opposed to alumina, as is expected for dust in circumstellar disks (see discussion above). Additionally SE > 8 for all but two spectra, indicating that most of our sample can be described as optically thin regions of amorphous silicate dust, which supports the model of Chiang & Goldreich (1997), in which the silicate feature arises from emission from an optically thin layer on disk surfaces. Following Egan & Sloan (2001), the other two sources, Hen 3-600A and HD 179218, which have the strongest emission at $\sim$11 μm, would be described as optically thick, but geometrically thin shells/disks of amorphous silicate dust. However, the SED for Hen 3-600A indicates optically thin dust and the spectra for both sources show sharp peaks at 11.2 μm, indicative of the presence of crystalline forsterite, rather than the smoother features expected from self absorption due to increased optical depth.

We also calculate IRAS colors as in Egan & Sloan (2001), using the zero-magnitude fluxes for

Table 5.6. Egan & Sloan calculations for selected sources.

Source	F_{10} Jy	F_{11} Jy	F_{12} Jy	index	[12]-[16]
LkCa 15	0.551	0.411	0.230	4.40	1.79
GM Aur	0.655	0.582	0.427	6.78	0.573
MWC 480	9.01	8.01	4.86	8.06	3.23
HD 163296	20.0	19.2	12.7	6.68	3.70
WW Vul	2.35	2.07	1.38	7.29	4.03
HD 184761	2.28	1.97	1.32	7.31	2.48
AA Tau	0.591	0.534	0.465	5.37	1.23
HD 179218	18.5	22.5	17.5	4.12	1.87
IRAS 14050-4109	0.226	0.183	0.114	8.22	1.95
Hen 3-600A	0.910	1.18	0.998	3.40	2.48

the non-color-corrected 12 and 25 μm IRAS filters (Cohen et al., 1992),

$$[12] - [25] = 2.5 \log \left(\frac{F_{\nu(25)}}{F_{\nu(12)}} \right) + 1.60. \tag{5.13}$$

The colors for our disks are in general much redder ($[12] - [25] > 1$) than those of AGB dust shells of the same spectral index, which contain much less dust. A notable exception is the disk around the T Tauri star GM Aur, which from the SED is expected to have been cleared of material within 4 AU of the central star, possibly due to planet formation (c.f. Rice et al., 2003).

The results of the Egan & Sloan analysis can be understood in terms of protoplanetary disks, through application of a physical model of disks which couples 2-D radiative transfer with the equation of vertical hydrostatics (Dullemond, 2002; Figure 5.13). In this model, the shape of the SED can be related to the radial and vertical optical depth of the disk. In Case A, the vertical and radial optical depth is large, the disk flares (causing increased flux in the SED at FIR wavelengths) and the inner region is shadowed by "puffed up inner wall" near the star (causing the 2 μm bump in the SED). Case B is similar to case A, with the added constraint that the disk remains radially optically thick at large radii and thus is self-shadowed. This does not change the shape of the SED, but may effect the size of the disk measured at millimeter wavelengths. For Case C, the vertical optical depth is small and the disk is not flared, but the radial optical depth is high enough to shadow the entire disk as shown in Figure 5.13 and the radiation in the SED decreases at long wavelengths ($\lambda \approx 50$ μm). Case D is a transparent disk for which both the vertical and radial optical depth is small and the SED falls off rapidly in the IR. Within the framework of this model, it is the hot grains in the inner disk that are being probed by the 10 μm silicate emission. The disks with SE > 8 represent the first scenario in which the flared disk results in a flat SED. This flared geometry is supported by observations of rotational transitions of the molecular gas in these disks

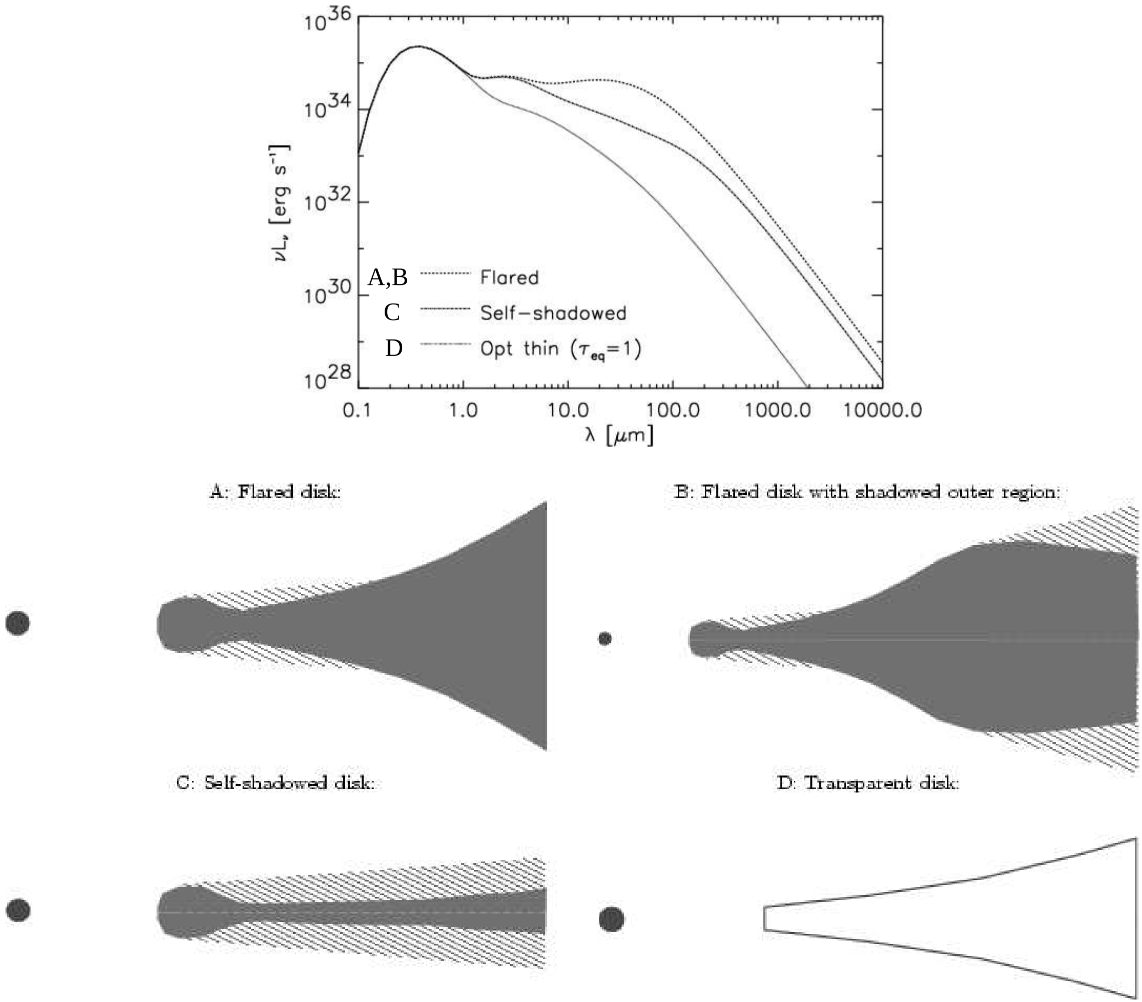

Figure 5.13 Cartoon of radiative transfer and vertical hydrostatic disk models (Dullemond, 2002). In this model, the shape of the SED is related to the radial and vertical optical depth of the disk. In models A and B, the disk is flared leading to shadowing of the inner and outer disk, respectively, and the SED is flat across FIR wavelengths. In model C, the vertical optical depth is small (no flaring), but the radial optical depth is high enough to keep the entire disk in shadow, reducing the radiation at $\sim$50 μm. Model D has low vertical and radial optical depth and thus the emission drops off rapidly in the IR.

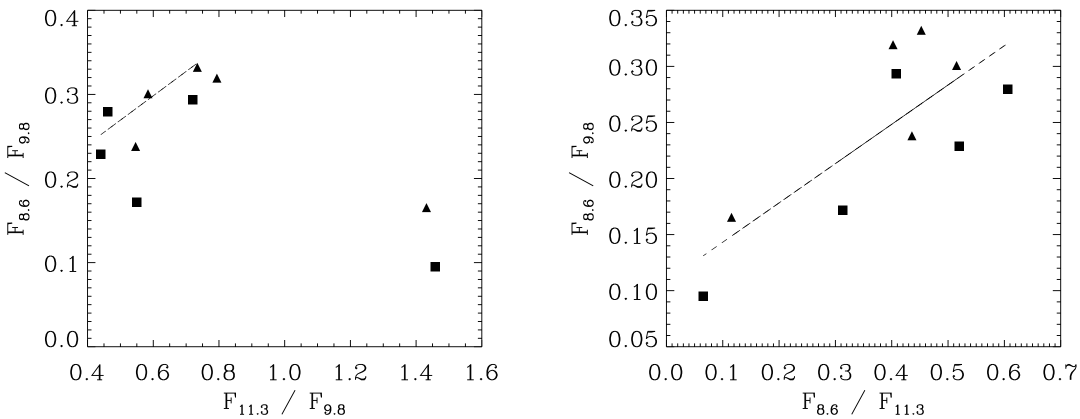

Figure 5.14 IR color-color diagrams. The first plot indicates the relationship between the slopes on the high $F_{11.3}/F_{9.8}$ and low wavelength $F_{8.6}/F_{9.8}$ side of the spectrum. The HD 179218 and Hen 3-600A are outliers, because they show substantial emission at 11.3 μm. The second plot shows the relationship between $F_{9.8}$ and $F_{11.3}$. The strengths of the two features appear to be linearly correlated, indicating that the flux at 11.3 μm does not grow at the expense of that at 9.8 μm, as would be expected if grains were being crystallized.

(specifically LkCa 15, GM Aur, MWC 480 and AA Tau; see Chapters 2 and 3), which indicate warm temperatures expected from additional heating by reprocessing of stellar radiation by dust in disk surface layers of flared disks. Surprisingly, however, the disk with the largest spectral index (SE$\sim$ 14), LkCa 15, is not expected to be the most flared and analysis of the SED indicates that much of the (large) circumstellar grains have settled to the disk midplane (Chiang et al., 2001). For Hen 3-600A and HD 179218, the low spectral indices indicate that the disk is vertically optically thin, but radially optically thick, shielding the outer disk from direct stellar radiation, so that these disks are less likely to be flared and more likely to be self shadowed. This is consistent with the SED for Hen 3-600A, but less so for that of HD 179218, as the flux is still quite high in the FIR.

5.7 Silicate emission feature and grain size

Here we discuss the relationship of the shape of the spectra with the grain size and composition. Van Boekel et al. (2003) examined the spectra from 12 Herbig Ae/Be stars and found that there is a correlation between the feature strength (peak-to-continuum flux) and shape (as indicated by the ratio of the flux at 11.2 to 8.9 μm), with broader emission features being weaker as shown in Figure 5.15 (open triangles). They also showed that the absorption coefficients of 0.1 and 2.0 μm olivine grains match the strong, narrow and broad, weak silicate emission, respectively, indicating that grain size can play a large role in determining the shape/strength of the emission feature.

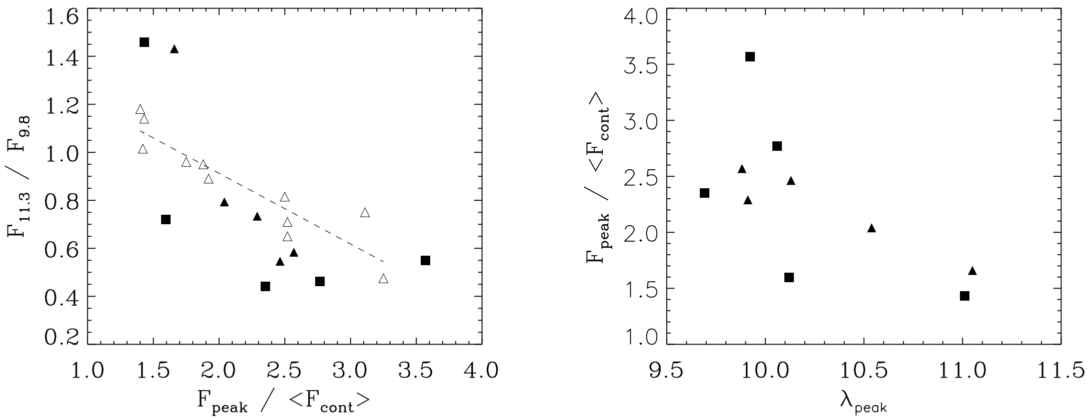

Figure 5.15 Feature characteristics. In both plots, the solid squares and triangles represent the observations of T Tauri and Herbig Ae/Be stars in our sample. The first plot shows the correlation between feature strength and shape, as noted in van Boekel et al. (2003). The dashed line is a linear fit to the van Boekel data set (open triangles). The second plot shows the strength of the silicate feature as a function of the wavelength at which the spectrum peaks. It appears that as the peak shifts to higher wavelengths, indicating larger percentages of crystalline silicates, the strength of the feature decreases.

The solid squares and triangles in Figure 5.15 represent the observations of T Tauri and Herbig Ae/Be stars in our sample. The dashed line is a linear fit to the van Boekel data set. The new data, for the most part, is roughly consistent with the previous trend (including the T Tauri stars). Previous studies of HAEBE stars by Bouwman et al. (2001) indicated that the trend depicted here is a function of both the size and crystallinity of the dust, and thus it is reasonable to think of the strong, narrow and the broad, weak silicate emission features as arising from"unprocessed" and "processed" dust, respectively. However, the two sources with spectra depicting significant emission at 11.3 μm possess stronger silicate features that would be expected to fit the trend found by van Boekel et al. (2003). This can easily be explained if the trend presented by van Boekel et al. (2003) arises primarily from variations in the size of the grains and the additional flux at 11.3 μm for Hen 3-600A and HD 179218 requires the presence of crystalline silicates. The contributions from dust size and composition can then be separated in this manner.

In Figure 5.15 the strength of the silicate feature is plotted with respect to the wavelength of the peak emission. As discussed above, the position of the peak emission likely corresponds to the degree of dust processing as the silicates change from predominantly amorphous olivine (9.7 μm) to enstatite (10.3 μm) to forsterite (11.3 μm). The plot indicates that as the peak position shifts from the classical shape to that of processed dust, the amount of emitting material decreases. 10 μm emission probes the warm, small (< 10 μm) dust grains at the disk surface within 5 AU of the star. The trend observed can thus be explained by a removal of small grains from the disk surface, either through grain growth (supported by the connection between grain growth and the flatness of the spectrum presented above), dust settling, or gap clearing. If the trend were related to removal of dust through gap clearing, then we would expect that GM Aur, which shows evidence of a substantial gap, would peak longward of 9.6 μm. It has also been suggested (Gail, 1998) that progressing crystallization should be accompanied by a drop in opacity of the dust material.

5.8 Spectra and SEDs

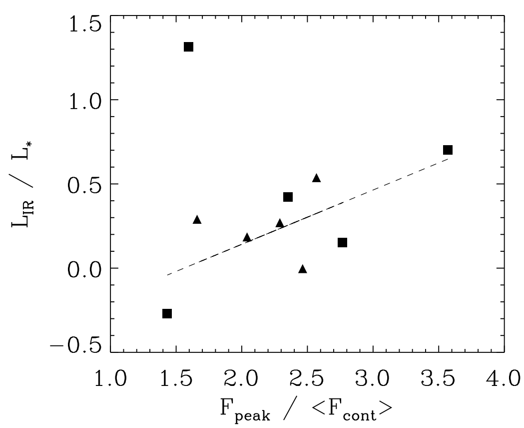

Figure 5.16 Correlations with the SED. This plot shows the correlation between the strength of the silicate feature and the IR-to-stellar luminosity ratio, a measure of the amount of dust in the disk. The outlier is AA Tau, for which the continuum could not be fit and was assumed to be flat at the flux of the 8 μm end of the spectrum.

In order to determine how the amount of warm disk material affects the strength and shape of the silicate emission feature, L_{IR}/L_{tot} and L_{IR}/L_* were calculated from the SEDs as described above. The fractional IR luminosity (L_{IR}/L_{tot}) was not found to be significantly correlated with the position of the ~10 μm silicate peak, indicating that the degree of silicate processing is not directly related to the amount of warm dust. The fact that the strength of the feature is correlated with the position of the peak, but the fractional IR luminosity is not, indicates that the former correlation is most likely due to a change in opacity of the dust, rather than a change in the number of grains. L_{IR}/L_* is found to be correlated to the strength of the emission feature (Figure 5.16), indicating that the amount of warm grains does effect the amount of silicates, if not the degree of dust processing.

5.9 Conclusions and future work

Spectra from 8–13 μm have been obtained for several low and intermediatemass YSOs. An evolutionary sequence from absorption in young, embedded sources, to emission in isolated stars and complete absence in older "debris" disks seen in ISO observations of high/intermediate mass YSOs (Meeus & Waelkens, 1999) was confirmed and extended here to $\sim$ solar mass stars. The shape of the silicate spectra of most T Tauri stars differed little from that toward the ISM, in contrast to the structured emission feature observed for most HAE stars. It is unclear whether crystalline silicates are truly absent in T Tauri stars, for colder or larger crystalline silicate grains would not emit in the 8–13 μm region, but may be visible through far-infrared lattice modes accessible from space born observations. The spectra obtained in this study were compared with other observations and it was found that variations in shape of the spectrum with time did not appear to be correlated with the evolutionary class of the star nor the shape of the silicate emission feature. For the objects with silicate in emission, the shape of the feature was evaluated using the quantitative method of Egan & Sloan (2001) and it was found to be consistent with optically thin disks of amorphous silicate (>80%) dust of geometries similar to those predicted by Dullemond (2002). We also find a correlation between the peak shape and feature strength for 4 TTs and 4 HAE in our sample, which is consistent with that found for 11 HAE stars by van Boekel et al. (2003), which they attribute to changes in grain size (from 0.1–2 μm). Two exceptions were the T Tauri star Hen 3-600A and the HAE star HD 179218, which both lie above the correlation and show strong emission at 11.3 μm, suggesting that the evolution of the silicate feature does not solely represent a change in grain size. Lastly, we found that the strength, but not the shape of the silicate emission feature was correlated with the fractional infrared luminosity (optical depth of the disk).

Due to sensitivity limitations, the ISO studies of silicates described above were confined to intermediate or high-mass stars. Silicate emission features in solar mass T-Tauri stars have only been observed from the ground, recently with the availability of 10m telescopes, in the 10 μm atmospheric window. SIRTF will greatly expand these studies. For example, a large sample of low mass stars, ranging from embedded protostars to optically thin disks, will be studied by the Evans ($\tau_{dust} > 1$) and Meyer ($\tau_{dust} < 1$) Legacy Science programs. In this manner, the study of the crystalline and amorphous silicates in disks, will be expanded to include disks around low mass, sun-like stars, creating a database analogous to ISO studies of high/intermediate-mass stars. These studies will include higher wavelength silicate bands, which depend intricately on the coordination of the silicon atoms and can provide more specific information about the minerals present, including the Mg/Fe ratio. The mineral content of the grains in each stage of evolution can thus be directly compared to that of meteorites, asteroids and comets.

Bibliography

Backman, D. E. & Paresce, F. 1993, in Protostars and Planets III, 1253–1304

Beichman, C. A., Neugebauer, G., Habing, H. J., Clegg, P. E., & Chester, T. J. 1988, NASA Reference Publication, 1190, 1

Berrilli, F., Corciulo, G., Ingrosso, G., Lorenzetti, D., Nisini, B., & Strafella, F. 1992, ApJ, 398, 254

Bouwman, J., de Koter, A., Dominik, C., & Waters, L. B. F. M. 2003, A&A, 401, 577

Bouwman, J., Meeus, G., de Koter, A., Hony, S., Dominik, C., & Waters, L. B. F. M. 2001, A&A, 375, 950

Chiang, E. I. & Goldreich, P. 1997, ApJ, 490, 368

Chiang, E. I., Joung, M. K., Creech-Eakman, M. J., Qi, C., Kessler, J. E., Blake, G. A., & van Dishoeck, E. F. 2001, ApJ, 547, 1077

Cohen, M., Emerson, J. P., & Beichman, C. A. 1989, ApJ, 339, 455

Cohen, M., Walker, R. G., & Witteborn, F. C. 1992, AJ, 104, 2030

Cohen, M. & Witteborn, F. C. 1985, ApJ, 294, 345

D'Alessio, P., Calvet, N., & Hartmann, L. 2001, ApJ, 553, 321

de La Reza, R., Torres, C. A. O., Quast, G., Castilho, B. V., & Vieira, G. L. 1989, ApJ, 343, 61

Dullemond, C. P. 2002, A&A, 395, 853

Egan, M. P. & Sloan, G. C. 2001, ApJ, 558, 165

Fabian, D., Henning, T., Jäger, C., Mutschke, H., Dorschner, J., & Wehrhan, O. 2001, A&A, 378, 228

Fajardo-Acosta, S. B., Knacke, R. F., & Telesco, C. M. 1993, Bulletin of the American Astronomical Society, 25, 1340

Finocchi, F. & Gail, H.-P. 1997, A&A, 327, 825

Finocchi, F., Gail, H.-P., & Duschl, W. J. 1997, A&A, 325, 1264

Friedemann, C., Guertler, J., & Reimann, H.-G. 1995, A&A, 300, 269

Gail, H.-P. 1998, A&A, 332, 1099

Geoffray, H. & Monin, J. L. 2001, A&A, 369, 239

Gibb, E. L., Whittet, D. C. B., Schutte, W. A., Boogert, A. C. A., Chiar, J. E., Ehrenfreund, P., Gerakines, P. A., Keane, J. V., Tielens, A. G. G. M., van Dishoeck, E. F., & Kerkhof, O. 2000, ApJ, 536, 347

Glass, I. S. 1975, MNRAS, 171, 19P

Grossman, L. 1972, GeCoA, 38, 47

Habing, H. J., Dominik, C., Jourdain de Muizon, M., Laureijs, R. J., Kessler, M. F., Leech, K., Metcalfe, L., Salama, A., Siebenmorgen, R., Trams, N., & Bouchet, P. 2001, A&A, 365, 545

Hanner, M. S., Brooke, T. Y., & Tokunaga, A. T. 1995, ApJ, 438, 250

—. 1998, ApJ, 502, 871

Hanner, M. S., Lynch, D. K., & Russell, R. W. 1994, ApJ, 425, 274

Hillenbrand, L. A., Strom, S. E., Vrba, F. J., & Keene, J. 1992, ApJ, 397, 613

Honda, M., Kataza, H., Okamoto, Y. K., Miyata, T., Yamashita, T., Sako, S., Takubo, S., & Onaka, T. 2003, ApJ, 585, L59

Jayawardhana, R., Fisher, R. S., Telesco, C. M., Piña, R. K., Barrado y Navascués, D., Hartmann, L. W., & Fazio, G. G. 2001, AJ, 122, 2047

Jura, M., Zuckerman, B., & Becklin, E. E.and Smith, R. C. 1993, ApJ, 418, 37

Kastner, J. H., Zuckerman, B., Weintraub, D. A., & Forveille, T. 1997, Science, 277, 67

Kenyon, S. J., Calvet, N., & Hartmann, L. 1993, ApJ, 414, 676

Kenyon, S. J. & Hartmann, L. 1987, ApJ, 323, 714

—. 1995, ApJ, 101, 117

Knacke, R. F., Fajardo-Acosta, S. B., Telesco, C. M., Hackwell, J. A., Lynch, D. K., & Russell, R. W. 1993, ApJ, 418, 440

Lawrence, G., Jones, T. J., & Gehrz, R. D. 1990, AJ, 99, 1232

Malfait, K., Yamamura, I., Waters, L. B. F. M., Tielens, A. G. G. M., de Graauw, M. S., de Jong, T., de Koter, A., Malfait, K., van den Ancker, M. E., Van Winckel, H., Voors, R. H. M., & Waelkens, C. 1999, Nature, 401, 563

Mannings, V. & Sargent, A. I. 1997, ApJ, 490, 792

—. 2000, ApJ, 529, 391

Meeus, G. & Waelkens, C. 1999, in ESA SP-427: The Universe as Seen by ISO, 373–+

Meeus, G., Waters, L. B. F. M., Bouwman, J., van den Ancker, M. E., Waelkens, C., & Malfait, K. 2001, A&A, 365, 476

Metchev, S. A., Hillenbrand, L. A., & Meyer, M. R. 2003, ArXiv Astrophysics e-prints

Miroshnichenko, A. S., Mulliss, C. L., Bjorkman, K. S., Morrison, N. D., Kuratov, K. S., & Wisniewski, J. P. 1999, MNRAS, 302, 612

Molster, F. J., Yamamura, I., Waters, L. B. F. M.and Tielens, A. G. G. M., de Graauw, T., de Jong, T., de Koter, A., Malfait, K., van den Ancker, M. E., Van Winckel, H., Voors, R. H. M., & Waelkens, C. 1999, Nature, 401, 563

Mouillet, D., Larwood, J. D., Papaloizou, J. C. B., & Lagrange, A. M. 1997, MNRAS, 292, 896

Myers, P. C., Fuller, G. A., Mathieu, R. D., Beichman, C. A., Benson, P. J., Schild, R. E., & Emerson, J. P. 1987, ApJ, 319, 340

Natta, A., Grinin, V. P., Mannings, V., & Ungerechts, H. 1997, ApJ, 491, 885

Natta, A., Meyer, M. R., & Beckwith, S. V. W. 2000, ApJ, 534, 838

Natta, A., Prusti, T., Neri, R., Wooden, D., Grinin, V. P., & Mannings, V. 2001, A&A, 371, 186

Nuth, J. A. & Donn, B. 1982, ApJ, 257, L103

Qi, C. 2001, PhD thesis, California Institute of Technology

Rice, W. K. M., Wood, K., Armitage, P. J., Whitney, B. A., & Bjorkman, J. E. 2003, MNRAS, 342, 79

Simon, M., Dutrey, A., & Guilloteau, S. 2001, ApJ, 545, 1034

Sitko, M. L., Grady, C. A., Lynch, D. K., Russell, R. W., & Hanner, M. S. 1999, ApJ, 510, 408

Skinner, C. J., Barlow, M. J., & Justtanont, K. 1992, MNRAS, 255, 31P

Skinner, C. J., Sylvester, R. J., Graham, J. R., Barlow, M. J., Meixner, M., Keto, E., Arens, J. F., & Jernigan, J. G. 1995, ApJ, 444, 861

Sloan, G. C. & Price, S. D. 1995, ApJ, 451, 758

—. 1998, ApJS, 119, 141

Sylvester, R. J., Skinner, C. J., Barlow, M. J., & Mannings, V. 1996, MNRAS, 279, 915

Thi, W. F., van Dishoeck, E. F., Blake, G. A., van Zadelhoff, G. J., Horn, J., Becklin, E. E., Mannings, V., Sargent, A. I., van den Ancker, M. E., Natta, A., & Kessler, J. 2001, ApJ, 561, 1074

van Boekel, R., Waters, L. B. F. M., Dominik, C., Bouwman, J., de Koter, A., Dullemond, C. P., & Paresce, F. 2003, A&A, 400, L21

van den Ancker, M. E., Bouwman, J., Wesselius, P. R., Waters, L. B. F. M., Dougherty, S. M., & van Dishoeck, E. F. 2000, A&A, 357, 325

van den Ancker, M. E., de Winter, D., & Tjin A Djie, H. R. E. 1998, A&A, 330, 145

Weinberger, A. J., Becklin, E. E., & Zuckerman, B. 2003, ApJ, 584, L33

White, R. J. & Ghez, A. M. 2001, ApJ, 556, 265

Wooden, D. H. 2002, Earth Moon and Planets, 89, 247

Zuckerman, B., Song, I., Bessell, M. S., & Webb, R. A. 2001, ApJ, 562, L87